Coupled electrochemical–mechanical model for fracture analysis in active materials of lithium ion batteries

Journal of Power Sources 580 (2023) 233378

Contents lists available at ScienceDirect

Journal of Power Sources

journal homepage: www.elsevier.com/locate/jpowsour

Coupled electrochemical–mechanical model for fracture analysis in active materials of lithium ion batteries

Francesca Pistorio *, Davide Clerici, Francesco Mocera, Aurelio Somà

Department of mechanical and aerospace engineering, Politecnico di Torino, Corso Duca degli Abruzzi, 24, 10129, Torino, Piemonte, Italy

GRAPHICAL ABSTRACT

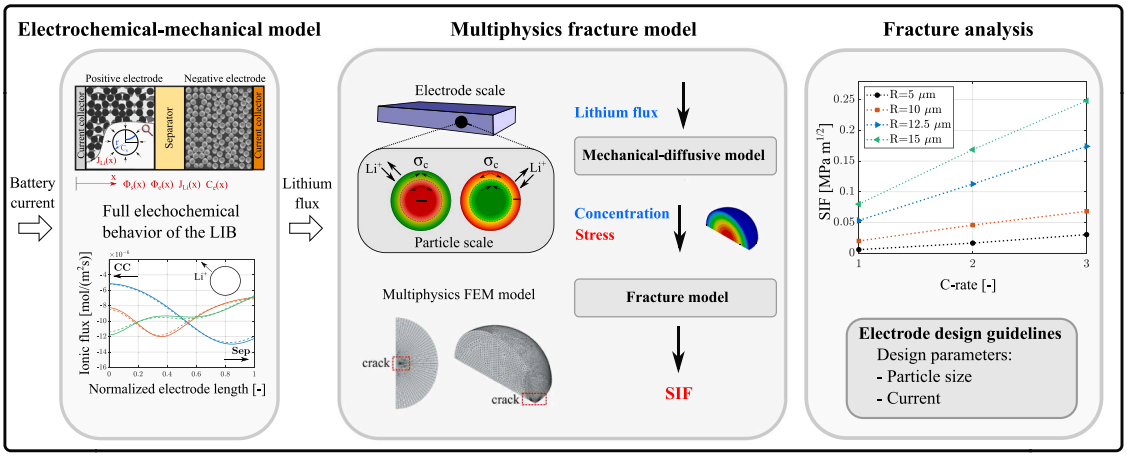

HIGHLIGHTS

- Coupled electrochemical–mechanical modeling of lithium ion battery.
- Mechanical-diffusive FEM model of active material particles with cracks.
- Fracture parameter computation for coupled electrochemical–mechanical problem.
- Realistic fracture predictions in microstructure of electrode layers.
- Damage prediction as a function of charge and discharge rate and geometric parameters.

ARTICLE INFO

Keywords:
Lithium ion batteries
Mechanical-diffusive coupling
Fracture mechanics
Finite element model
Stress intensity factor

ABSTRACT

Mechanical degradation is a significant cause of battery aging: the stress arising in the electrode microstructure during operation causes fractures, leading to capacity and power fade. This work aims to quantify the fracture behavior of LCO-graphite battery by computing the stress intensity factor. At first, the full electrochemistry of the cell is modeled to obtain realistic boundary conditions for the fracture model linked to user-defined battery usage. The fracture model of a spherical active material particle is implemented in Ansys to compute stress intensity factor with modified J-integral for mechanical-diffusive phenomena. Three aspects are deepened: (a) The effects of the mechanical-diffusive coupling at the crack tip, and its influence on the stress intensity factor; (b) Assessing fracture propagation due to static loading and its stability; (c) Creating a fracture diagram which quantifies the level of fracture due to the combination of different operating conditions and geometry of the

* Corresponding author.
E-mail address: francesca.pistorio@polito.it (F. Pistorio).

https://doi.org/10.1016/j.jpowsour.2023.233378
Received 19 April 2023; Received in revised form 27 June 2023; Accepted 29 June 2023
Available online 8 August 2023

electrode microstructure. Results show that crack propagation in a single cycle is limited to high current, but it is likely to be unstable. Furthermore, it is quantified how greater current and particle radius increase the stress intensity factor, aiming to provide electrode design advice in the perspective of increasing battery life.

1. Introduction

Lithium ion batteries (LIBs) are one of the most widespread rechargeable energy storage systems. LIBs are extensively employed in many applications, from portable electronics up to working vehicles, due to their good characteristics in terms of energy and power density, safety, and cycle life [1–4].

In recent years, advanced materials and manufacturing processes have been developed in order to increase energy density and limit capacity and power loss during life. Nonetheless, progressive damage caused by repeated charge–discharge cycles is still a significant weak point, since it considerably affects the lifetime and results in a decrease of the nominal performance [5–7]. Therefore, a deep understanding of aging mechanisms is needed to develop high-capacity LIBs with a long life cycle and meet the rapidly growing demand for high-performance rechargeable energy storage systems.

LIBs consist of several "elementary cells", made of thin layers (≈μm) of current collectors, cathode, anode, and separator. Cathode and anode are composite materials made of active material, namely a powder of quasi-spherical particles (≈ 50% v/v) in which lithium is extracted and inserted, conductive materials and binder (≈20% v/v), and voids (≈30% v/v) filled with the electrolyte which soaks active material and provides a continuous pathway to conduct lithium ions.

Lithium ions move between electrodes and get into their microstructure with insertion and extraction processes. Lithium diffusion within active material particles induces an inhomogeneous concentration distribution. Areas with higher lithium concentration show a greater deformation than areas with lower concentration, then a strain mismatch arises in particles, leading to the so-called diffusion induced stress (DIS) [8–13].

DIS may cause the fracture of the electrode microstructure, leading to the isolation of active material and the creation of new surfaces where the solid electrolyte interphase (SEI) layer grows, resulting in impedance rise and capacity fade ultimately.

Impedance rise is caused by the interruption of the ions pathway due to the contact loss between the active material and conductive matrix or current collector. On the other hand, capacity fade is caused by the isolation of some portion of active material, being inactive and no longer able to host lithium ions, and by the growth of the SEI layer, whose reaction consumes lithium ions, which are no longer available to be cycled [14–16].

The stress field and fracture in active material particles are strongly coupled to lithium concentration distribution. Indeed, several studies modeling single, spherical isolated active material particles demonstrated that the stress is significantly overestimated when neglecting the mechanical-diffusive coupling [10,12,17–19]. Furthermore, both numerical [20–23] and experimental works [24] demonstrated that lithium concentration is affected by the crack presence due to the higher stress at the crack tip.

Several fracture mechanisms were reported in the literature according to the type of active material. Comprehensive reviews [25,26] dealt with the experimental characterization of the fracture mechanisms in the most popular active materials used in LIBs, as well as the factors triggering and enhancing fracture. In these works, it is observed that the crack mainly

propagates according to mode-I because of tensile hoop stress [27–29].

In the last years, several numerical models have been developed to describe fracture occurring in the electrode microstructure. These models have been generally implemented using the finite element model (FEM) and eXtended finite element model (XFEM), as the analytical approach can be used just in the case of simple geometry and loading conditions [30].

Linear elastic fracture mechanics (LEFM) model is widely employed to describe fracture in active material particles with pre-existent defects. Based on LEFM, several works studied crack propagation according to the stress intensity factor (SIF) criterion [31–35] or the energetic approach, evaluating the energy release rate G. In

the latter case, the energy release rate G is often computed using the path-independent J-integral formulation developed for diffusive-mechanical phenomena [36–38].

Alternatively to the LEFM model, the cohesive zone model (CZM) [23,39–46] as well as the phase field model (PFM) [47–57] are employed, even without assuming pre-existent cracks [43].

Most of the studies predicted fracture considering free standalone active material particles, according to the single-particle-model (SPM) approach. However, active material particles are components of a larger complex system of interacting species. Although the SPM simplifies the numerical modeling and computation, its prediction of lithium concentration, stress field, and mechanical failure may be not realistic and substantially different from the one obtained considering the full LIB electrochemistry.

The pseudo-two-dimensional electrochemical model (P2D) originally developed by Newman's group [58] has been extensively used to fully model LIB electrochemistry. P2D simulates the electrode microstructure according to the porous electrode theory and assumes spherical active material particles with a uniform size placed along the thickness of the electrode. Two different length scales are employed to simulate lithium transport, namely the electrode scale and the particle scale.

As far as the authors know, no prior works in the literature considered both the effect of mechanical-diffusive coupling and the full electrochemistry of LIB when modeling fracture in active material particles.

This works aims to fill this gap and provide a more realistic prediction of the fracture behavior of active materials of electrodes. Then, a coupled multi-physics and multi-scale framework is developed, where the results of the P2D model are the boundary condition of the mechanical-diffusive fracture model at the particle scale. Fracture parameters, namely the J-integral and mode-I SIF are computed in spherical particles with pre-existent defects. A discussion on the mutual interaction between lithium transport, DIS, and fracture due to the mechanical-diffusive coupling is provided. Furthermore, the crack growth stability is studied. Finally, the effect of the current rate and the particle size on the fracture behavior is evaluated with the purpose of giving practical suggestions in the electrode design to limit mechanical degradation.

The article is organized as follows. The basis of the P2D model and the formulation of a path-independent J-integral for coupled mechanical-diffusive problems are presented in Section 2.1. The multi-physics and multi-scale model developed to analyze fracture in active material particles is presented in Section 2.2. The results of the model applied to LCO-graphite LIB are shown in Section 3.

2. Methods

2.1. Theoretical modeling

2.1.1. Electrochemical–mechanical model

In this work, LIB electrochemistry is modeled on the basis of the P2D model, consisting of a set of partial differential and algebraic

Nomenclature

Symbols

a	Crack length (μm)
a_s	Particle surface area to volume (mol/m^3)
c	Concentration (mol/m^3)
C_p	Specific heat capacity (J/(kgK))
D	Diffusion coefficient (m^2/s)
E	Young modulus (MPa)
E_a	Activation energy (J)
F	Faraday constant (As/mol)
I	Current density (A/m^2)
J_{Li}	Lithium flux (mol/m^{2}s)
k	Reaction rate constant (m$^{2.5}$/mol$^{0.5}$s)
K_I	Mode-I stress intensity factor (MPa m$^{0.5}$)
k_m	Mechanical coupling parameter (m^3/mol)
K_{Ic}	Mode-I fracture toughness (MPa m$^{0.5}$)
K_{IIc}	Mode-II fracture toughness (MPa m$^{0.5}$)
K_{IIIc}	Mode-III fracture toughness (MPa m$^{0.5}$)
K_{III}	Mode-III stress intensity factor (MPa m$^{0.5}$)
K_{II}	Mode-II stress intensity factor (MPa m$^{0.5}$)
l	Thickness (μm)
n_i	Normal versor (–)
q	Crack extension vector (μm)
Q_{ohm}	Ohmic heat (J)
Q_{rev}	Reversible heat (J)
Q_{rxn}	Reaction heat (J)
R	Active material particle radius (μm)
r	Radial coordinate (–)
R_g	Gas constant (J/mol K)
T	Temperature (K)
t	Time (s)
t_i	Traction vector (MPa)
t_+	Trasference number (–)
U	Open Circuit Voltage (V)
u	Particle level displacement (μm)
W	Strain energy density (J/m^3)
x	Electrode through-thickness coordinate
x_1	Coordinate direction along crack extension
x_2	Coordinate direction perpendicular to crack extension
h	Heat exchange coefficient (W/m^2 K)

Acronyms

CZM	Cohesive zone model
DAE	Differential algebraic equation
DIS	Diffusion induced stress
DOD	Depth of discharge (%)
FEM	Finite element model
FVM	Finite Volume Method
LCO	Lithium cobalt oxide
LEFM	Linear elastic fracture mechanics
LIB	Lithium ions battery
P2D	Pseudo-two-dimensional model
PDAE	Partial differential algebraic equation
PFM	Phase field model
SEI	Solid electrolyte interphase
SIF	Stress intensity factor
SOC	State of charge (%)
SPM	Single particle model
XFEM	Extended finite element model

Greek Symbols

α	Expansion coefficient (1/K)
ϵ^c	Diffusion strain (–)
ϵ^T	Thermal strain (–)
ϵ_c	Hoop strain (–)
ϵ_e	Porosity (–)
ϵ_f	Filler fraction (–)
ϵ_r	Radial strain (–)
η	Overpotential (V)
Γ	Path
κ_e	Electrolyte conductivity (S/m)
Λ	Area enclosed in the path Γ
λ	Thermal conductivity (W/(mK))
ν	Poisson ratio (–)
Ω	Partial molar volume (m^3/mol)
Φ	Potential (V)
ρ	Density (kg/m^3)
σ	Solid conductivity (S/m)
σ_c	Hoop stress (MPa)
σ_h	Hydrostatic stress (MPa)
σ_r	Radial stress (MPa)
θ	Stoichiometric limit (–)

Recursive subscripts

e	Electrolyte
e,n	Electrolyte in anode
e,p	Electrolyte in cathode
e,s	Electrolyte in separator
n	Anode
p	Cathode
s	Separator
s,n	Solid-phase in anode
s,p	Solid-phase in cathode
eqv	Equivalent

Recursive superscripts

Eff	Effective
max	Maximum
surf	Surface

equations (PDAEs) for charge and mass conservation. These equations are solved within an elementary cell of the LIB, composed of a cathode, a separator, and an anode.

The P2D model assumes that the electrode active material is represented by spherical particles with uniform size, then two scales are involved: the electrode and particle scales, as shown in Fig. 1a.

The time variable t and two independent spatial variables are involved in the P2D model, i.e. the coordinate in the direction across the cell thickness (x) and the coordinate along the particle radial direction (r).

At the electrode scale, the following equations governing electrons and lithium transport across the cell thickness are written: (1) charge conservation equation, involving potentials in active material ($\Phi_{s,p}$

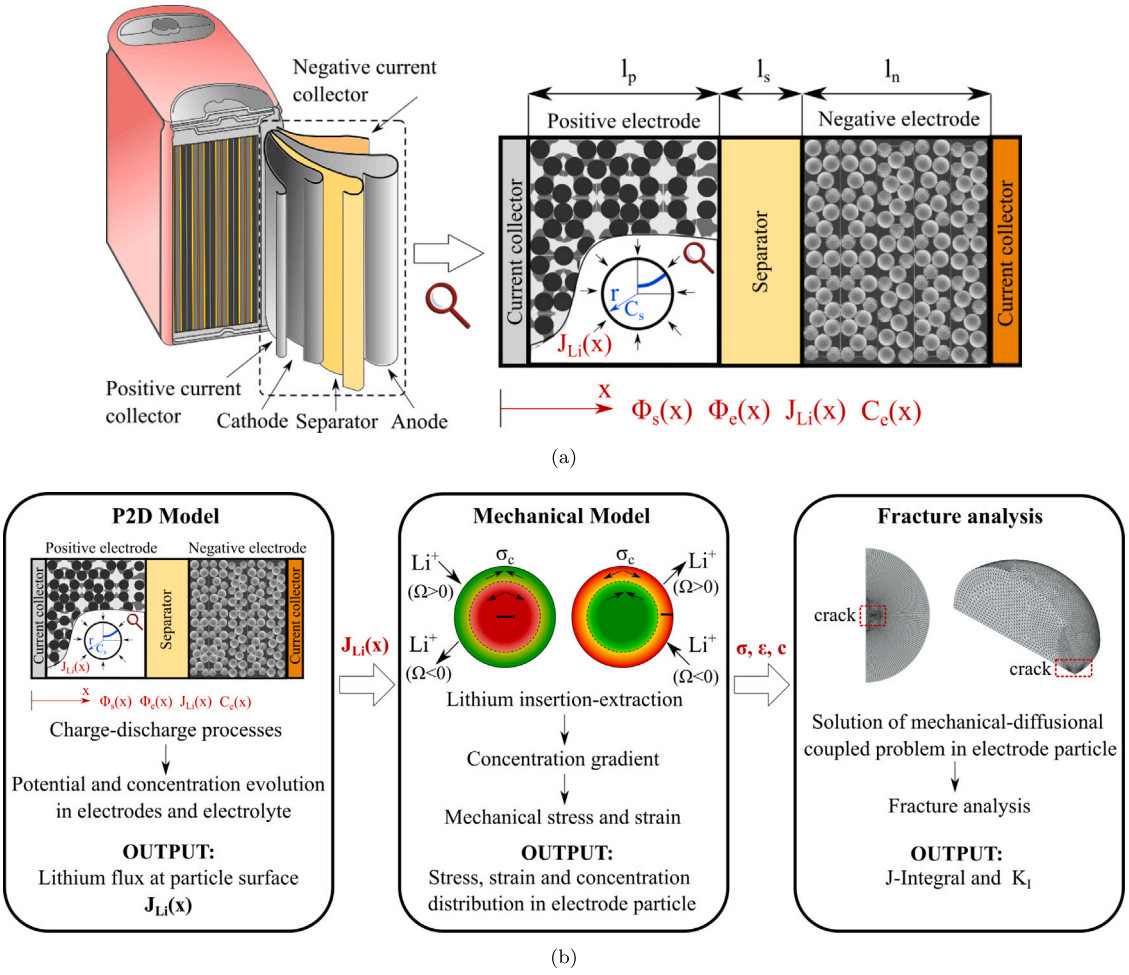

Fig. 1. (a) LIB internal structure with detail of the cross section of an elementary cell. The elementary cell is modeled according to the electrode (x-through-plane direction) and particle (r-radial direction) scales. The quantities involved at the electrode scale and particle scale are depicted in red and blue, respectively. (b) Multi-scale and multi-physics modeling framework simulating fracture in electrode active material, capturing the full coupling between lithium diffusion, stress, and fracture.

and $\Phi_{s,n}$) and electrolyte ($\Phi_{e,p}$, $\Phi_{e,s}$ and $\Phi_{e,n}$); (2) mass conservation equation, involving electrolyte concentration ($c_{e,p}$, $c_{e,s}$, $c_{e,n}$), where the subscripts p, s and n stand for cathode, separator, and anode, respectively.

The charge transfer reaction is captured by imposing the same current density at the interface between the particles and electrolyte. Indeed, once lithium ions reach the surface of the particles, they are neutralized by electrons with a charge transfer reaction and subsequently diffuse into the particles. The charge transfer reaction is modeled by the Butler-Volmer equation, which establishes the link between the electrode and particle scales, relating the potentials ($\Phi_{s,p}$, $\Phi_{e,p}$ and $\Phi_{s,n}$, $\Phi_{e,n}$) at electrode scale to the lithium flux over active material particles ($J_{Li,p}$ and $J_{Li,n}$) at particle scale.

At the particle scale, the mass conservation equation governs lithium diffusion within the particle. It is a 1D equation written as a function of the particle radial coordinate (r) thanks to the symmetry of the geometry (spherical particle), boundary conditions, and the hypothesis of homogeneous and isotropic material.

The complete set of governing equations of the P2D model are reported in Appendix A.

Lithium transport in active materials is a coupled multi-physics process. Diffusive and mechanical fields are linked by the chemical strain $\left(\frac{\Omega_k \overline{c_{s,k}}}{3}\right)$, which is the term added to the elastic strain components in Eq. (1)a. Furthermore, mechanical and diffusive phenomena influence each other [10–12]: the (de)intercalation of lithium ions gives rise to an inhomogeneous concentration distribution in active material particles, causing differential strain and stress. The latter affects how lithium ions diffuse in turn, making the two fields coupled.

Strain, stress, and displacement in active material particles caused by lithium concentration ($c_{s,k}$) are computed using the constitutive, congruence, and equilibrium equations reported in Eqs. (1)a–d.

Constitutive:

$$\varepsilon_r = \frac{1}{E_k}(\sigma_r - 2\nu_k\sigma_c) + \frac{\Omega_k\overline{c_{s,k}}}{3};\quad \varepsilon_c = \frac{1}{E_k}[(1-\nu_k)\sigma_c - \nu_k\sigma_r) + \frac{\Omega_k\overline{c_{s,k}}}{3} \tag{1a}$$

Congruence:

$$\varepsilon_r = \frac{\partial u}{\partial r};\quad \varepsilon_c = \frac{u}{r} \tag{1b}$$

Equilibrium:

$$\frac{\partial \sigma_r}{\partial r} + \frac{2}{r}(\sigma_r - \sigma_c) = 0 \tag{1c}$$

Boundary conditions:

$$u\Big|_{r=0} = 0;\quad \frac{\partial \sigma_r}{\partial r}\Big|_{r=R_k} = 0 \tag{1d}$$

Where the subscript $k = p, n$ refers to cathode and anode respectively, σ_r, ε_r, σ_c, ε_c are radial and circumferential stresses and strains respectively, u is the radial displacement, $\overline{c_{s,k}}$ is the lithium concentration net of zero-strain concentration, Ω_k is the partial molar volume of lithium ions, ν_k is the Poisson ratio, E_k is the Young modulus and R_k is the particle radius.

The mass conservation equation describing lithium transport in active material particles is reported in Eq. (2) [59].

$$\begin{cases} \frac{\partial c_{s,k}}{\partial t} = \frac{D_{s,k}}{r^2}\frac{\partial}{\partial r}\left(r^2\frac{\partial c_{s,k}}{\partial r} - r^2\frac{\Omega_k \overline{c_{s,k}}}{R_g T}\frac{\partial \sigma_h}{\partial r}\right) \\ D_{s,k}\left(\frac{\partial c_{s,k}}{\partial r} - \frac{\Omega_k \overline{c_{s,k}}}{R_g T}\frac{\partial \sigma_h}{\partial r}\right)\Big|_{r=0} = 0 \qquad \text{for t} \geq 0 \\ D_{s,k}\left(\frac{\partial c_{s,k}}{\partial r} - \frac{\Omega_k \overline{c_{s,k}}}{R_g T}\frac{\partial \sigma_h}{\partial r}\right)\Big|_{r=R_k} = -J_{Li,k} \qquad \text{for t} \geq 0 \end{cases} \tag{2}$$

Where $D_{s,k}$ is the diffusion coefficient, R_g is the gas constant, T is the temperature, $a_{s,k}$ is the particle surface area to volume, and $\sigma_h = \frac{\sigma_{11}+\sigma_{22}+\sigma_{33}}{3} = \frac{\sigma_r+2\sigma_c}{3}$ is the hydrostatic stress. Eq. (2) shows that mechanics and diffusive fields are coupled through the gradient of hydrostatic stress ($\frac{\partial \sigma_h}{\partial r}$), which is the additional term multiplying the diffusion coefficient ($D_{s,k}$) in Eq. (2). Then, both hydrostatic stress and concentration gradients are the driving force for lithium diffusion.

The mass conservation equation expressed in Eq. (2) is rewritten just as a function of lithium concentration ($c_{s,k}$) as reported in Eq. (4), by substituting the hydrostatic stress gradient ($\frac{\partial \sigma_h}{\partial r}$) expressed in Eq. (3).

$$\frac{\partial \sigma_h}{\partial r} = \frac{\partial \sigma_h}{\partial c_{s,k}}\frac{\partial c_{s,k}}{\partial r} = -\frac{2\Omega_k E_k}{9(1-\nu_k)}\frac{\partial c_{s,k}}{\partial r} \tag{3}$$

$$\begin{cases} \frac{\partial c_{s,k}}{\partial t} = D_{s,k}\left[\frac{\partial^2 c_{s,k}}{\partial r^2} + \frac{2}{r}\frac{\partial c_{s,k}}{\partial r} + k_m\left(\frac{\partial c_{s,k}}{\partial r}\right)^2 + k_m\overline{c_{s,k}}\left(\frac{\partial^2 c_{s,k}}{\partial r^2} + \frac{2}{r}\frac{\partial c_s}{\partial r}\right)\right] \\ \frac{\partial c_{s,k}}{\partial}\Big|_{r=0} = 0 \qquad \text{for t} \geq 0 \\ D_{s,k}\left(1 + k_m c_{s,k}\right)\frac{\partial c_{s,k}}{\partial r}\Big|_{r=R_k} = -J_{Li,k} \qquad \text{for t} \geq 0 \end{cases} \tag{4}$$

Where $k_m = \frac{\Omega_k}{R_g T}\frac{2\Omega_k E_k}{9(1-\nu_k)}$ is the parameter representing the coupling between mechanical and diffusive fields.

Eq. (4) is included in the P2D model to solve the concentration field. The solution of displacement, stress, and strain is obtained solving Eqs. (1)a–d, and is reported in Eqs. (5)a–c [59]. These quantities can be computed once the lithium concentration distribution resulting from the P2D model is known.

Displacement:

$$u(r) = \frac{\Omega_k}{3(1-\nu_k)}\left[(1+\nu_k)\frac{1}{r^2}\int_0^r \overline{c_{s,k}}(r) r^2\, dr + 2(1-2\nu_k)\frac{r}{R_k^3}\int_0^{R_k}\overline{c_{s,k}}(r) r^2\, dr\right] \tag{5a}$$

Radial stress:

$$\sigma_r(r) = \frac{2\Omega_k}{3}\frac{E_k}{1-\nu_k}\left[\frac{1}{R_k^3}\int_0^{R_k}\overline{c_{s,k}}(r) r^2\, dr - \frac{1}{r^3}\int_0^r \overline{c_{s,k}}(r) r^2\, dr\right] \tag{5b}$$

Hoop stress:

$$\sigma_c(r) = \frac{\Omega_k}{3}\frac{E_k}{1-\nu_k}\left[\frac{2}{R_k^3}\int_0^{R_k}\overline{c_{s,k}}(r) r^2\, dr + \frac{1}{r^3}\int_0^r \overline{c_{s,k}}(r) r^2\, dr - \overline{c_{s,k}}(r)\right] \tag{5c}$$

2.1.2. J-integral for coupled mechanical-diffusive problem

The J-integral is a fracture mechanics parameter widely used to characterize the stress–strain field at the crack tip in both linear and non-linear elastic material. According to LEFM theory, the J-integral is equal to the energy release rate G, i.e. the rate of decrease in potential energy per unit of surface created by the crack extension.

The J-integral proposed by Rice [60] for a 2D fracture problem is the contour integral expressed in Eq. (6), considering an arbitrary counterclockwise path Γ surrounding the crack tip (Figure S1 in Supplementary material).

$$J = \int_\Gamma\left(W dx_2 - \mathbf{t}\cdot\frac{\partial \mathbf{u}}{\partial x_1}\, ds\right) \tag{6}$$

Where $W = \int_0^{\epsilon_{ij}}\sigma_{ij} d\epsilon_{ij}$ (Einstein notation) is the strain energy density, σ_{ij} and ε_{ij} are the components of the stress and strain tensors, $\mathbf{u}$ is the displacement vector, $\mathbf{t}$ is the traction vector acting on the path Γ and its components are $t_i = \sigma_{ij} n_j$, n_j is the versor normal to Γ, x_1 and x_2 are the coordinate directions, and ds is the element length along the path Γ.

Eq. (6) states that the total energy inside the contour Γ, accounted by the first term of the line integral, is caused by the mechanical work done by the traction acting on the contour Γ, accounted by the second term of the line integral.

The J-integral expressed in Eq. (6) is path-independent, meaning that its value does not depend on the chosen path Γ, and it is equal to the energy release rate when the LEFM theory holds.

Previous works [36–38] demonstrated that the standard form of J-integral expressed in Eq. (6) is unsuitable for coupled fracture mechanical-diffusive problems because the J-integral is no longer path-independent when both chemical and mechanical driving forces are present at the same time. Similarly, the standard form of J-integral expressed in Eq. (6) is no longer path-independent in thermo-mechanical fracture problems.

A modified form of J-integral keeping the path-independence property in thermo-mechanical fracture problem (J_{MT}) was proposed by Aoki et al. [61] and Kishimoto et al. [62] and is expressed in Eq. (7).

$$J_{MT} = \int_\Gamma\left(W dx_2 - \mathbf{t}\cdot\frac{\partial \mathbf{u}}{\partial x_1}\, ds\right) + \int_\Lambda\left(\boldsymbol{\sigma}^P\cdot\frac{\partial \boldsymbol{\varepsilon}^T}{\partial x_1}\, d\Lambda\right) \tag{7}$$

Where Λ is the area enclosed by the path Γ, $\boldsymbol{\sigma}^P = [\sigma_{11}, \sigma_{22}, \sigma_{33}]$ is the vector of principal stresses, $\boldsymbol{\varepsilon}^T = \alpha\overline{T}$ is the thermal strain vector, α is the thermal expansion coefficient, and $\overline{T}$ is the temperature variation measured from the reference state. Then, the area integral in Eq. (7) involves a scalar product between the principal stress vector and the rate of change of the thermal strain vector with respect to the direction of crack extension (x_1).

A modified expression of J-integral for coupled mechanical-diffusive fracture problem (J_{MD}) is derived from Eq. (7) by exploiting the analogy between chemical and thermal deformation equations.

Chemical and thermal deformation are computed as the change of the field (concentration or temperature) with respect to the strain-free condition, times a coefficient of proportionality. The chemical and thermal deformations are isotropic, and their components are reported in Eq. (8) [10,12,35].

$$\varepsilon^c = \frac{\Omega}{3}[\overline{c}_s, \overline{c}_s, \overline{c}_s] \tag{8a}$$

$$\varepsilon^T = \alpha[\overline{T}, \overline{T}, \overline{T}] \tag{8b}$$

Where $\overline{T}$ is the temperature net of zero-strain temperature and α is the coefficient of thermal expansion.

Then, since the chemical deformation equation has the same shape of thermal deformation, it can be replaced in the J-integral formulated for thermal strain (Eq. (7)), resulting in Eq. (9).

$$J_{MD} = \int_\Gamma\left(W dx_2 - \mathbf{t}\cdot\frac{\partial \mathbf{u}}{\partial x_1}\, ds\right) + \int_\Lambda\left(\Omega\sigma_h\frac{\partial \overline{c}_s}{\partial x_1}\, d\Lambda\right) \tag{9}$$

Where σ_h is the sum of the three principal stress divided by three.

The first term on the right-hand side of Eq. (9) is the standard J-integral expression developed by Rice (Eq. (6)), and the second term accounts for the energy related to the deformation caused by lithium diffusion, which needs to be taken into account to satisfy the energy balance and to ensure the path-independence property of J-integral.

2.2. Multiphysics modeling

In this section, the multi-scale and multi-physics modeling framework employed to analyze the fracture in active material particles is presented.

Electrochemistry at the electrode level, the mechanical-diffusive coupling and fracture mechanics at the particle level, are modeled

Table 1
Hoop stress sign in active material particle during LIB charge/discharge. The positive and negative sign of σ_c refers to tensile and compressive hoop stress respectively, and R_p and R_n are the radii of particles in cathode and anode, respectively.

	Cathode				Anode	
	$\Omega > 0$		$\Omega < 0$		$\Omega > 0$	
Particle region	$r = 0$	$r = R_p$	$r = 0$	$r = R_p$	$r = 0$	$r = R_n$
Charge	$\sigma_c < 0$	$\sigma_c > 0$	$\sigma_c > 0$	$\sigma_c < 0$	$\sigma_c > 0$	$\sigma_c < 0$
Discharge	$\sigma_c > 0$	$\sigma_c < 0$	$\sigma_c < 0$	$\sigma_c > 0$	$\sigma_c < 0$	$\sigma_c > 0$

using three different submodels, according to the procedure reported in Fig. 1b and summarized as follows.

- **P2D model.** It computes the full electrochemical behavior of the LIB, solving the potential and lithium concentration distribution within the active material particles and the electrolyte. The coupling between mechanical and diffusive phenomena is considered according to Eq. (4). The output of the model is the lithium flux (J_{Li}) on the surface of the active material particles without pre-existent cracks.
- **Mechanical-diffusive model of cracked particle.** Given the lithium flux computed with P2D as boundary condition, it gives the lithium concentration distribution, strain, and stress within active material particles with pre-existent cracks. The model takes into account the coupling between stress at the crack tip and lithium diffusion.
- **Fracture model.** It gives fracture parameters, i.e. J-integral and mode-I SIF (K_I), on the basis of the stress and concentration fields calculated with the mechanical-diffusive model of cracked particle.

2.2.1. P2D model: LIB electrochemistry

The governing set of partial differential equations (PDEs) of the P2D model reported in Appendix A is solved using the open-source Li-ION SIMulation BAttery Toolbox (LIONSIMBA) [63].

LIONSIMBA is a set of customizable MATLAB functions suitable for the simulation of LIBs and battery packs. The governing equations of the P2D model are spatially discretized using the Finite Volume Method (FVM) and converted into a set of differential algebraic equations (DAEs). The resulting system of DAEs is solved using the time adaptative Implicit Differential-Algebraic (IDA) solver of the SUNDIALS integration suite. The modified mass conservation equation (Eq. (4)) is incorporated into the set of PDEs to take into account the influence of mechanical-diffusive coupling. The reader can refer to [63] for further details about the LIONSIMBA implementation.

The ionic flux on the surface of active material particles (J_{Li}) computed with LIONSIMBA is imposed as boundary condition of the multi-physics fracture FEM model in order to get the fracture behavior of the active material due to a realistic operating condition of the LIB.

2.2.2. Mechanical-diffusive particle model: FEM model of active material particle with pre-existent crack

Pre-existent defects in active material particles can propagate due to DIS generated during LIB operation. In this work, spherical particles with central and superficial cracks are modeled and mode-I crack propagation driven by tensile hoop stress is considered.

The largest tensile hoop stress occurs at the particle surface when the particle swells and in the core when the particle shrinks. Particle swelling or shrinkage is caused by lithium insertion or extraction according to the type of active material, namely whether the partial molar volume (Ω) is positive or negative. Table 1 summarizes the sign of the hoop stress in active material particles during LIB charge/discharge based on the sign of Ω.

In the model, the pre-existent crack is located in the particle region where the hoop stress is tensile, namely at the center during lithium insertion ($\Omega > 0$) or extraction ($\Omega < 0$) and at the surface during lithium extraction ($\Omega > 0$) or insertion ($\Omega < 0$), according to Table 1.

The central crack is disk-shaped with a diameter of $2a$ (Figure S2a), on the other hand, the superficial crack is a semi-circle with crack depth of a (Figure S2b). A 2D model is built for the spherical particle with the central crack exploiting the axisymmetry, on the other hand, a 3D model is needed for the particle with the superficial crack.

The influence of the crack on stress and concentration is simulated with a coupled mechanical-diffusive FEM model implemented in Ansys Mechanical APDL. Coupled field elements with both mechanical and diffusive degrees of freedom are used, i.e. PLANE223 and SOLID226 for 2D and 3D models, respectively. Mechanical stress and lithium concentration fields inside the particle are obtained simultaneously, according to the migration model implemented in Ansys [11].

The detailed description of the strategy followed to build the FEM model and the mesh is provided in Section S2 of Supplementary material.

The lithium flux (J_{Li}) computed with the P2D model according to the user-defined LIB operation is applied as electrochemical boundary condition in the FEM model. Then, stress and lithium concentration are calculated, considering the influence of the crack.

2.2.3. Fracture model: fracture parameters computation

A subsequent fracture analysis is performed in Ansys to compute fracture parameters. Then, the same mesh pattern employed in the mechanical-diffusive model is kept, and coupled fields PLANE223 and SOLID226 elements are converted into their corresponding structural elements which support fracture parameters computation, i.e. PLANE183 and SOLID186 respectively.

The path-independent J-integral for mechanical-diffusive fracture problem (J_{MD}) is computed using the concentration and stress distribution previously obtained using the migration model.

Ansys APDL offers the built-in command CINT to compute the J-integral directly at the solution phase of the analysis, using the domain integral formulation implemented by Shih [64]. The domain integral formulation converts the line J-integral into an area integral for 2D model and volume integral for 3D model. This ensures higher accuracy compared to the line integral as well as it is easier to implement numerically in FEM code.

The domain integral formulation for 2D model is reported in Eq. (10), neglecting body force and crack face traction and including the thermal strains contribution ($\alpha\sigma_{ii}\frac{\partial \overline{T}}{\partial x_1}$) beside the elastic contribution. Summation over repeated indices is employed according to the Einstein notation.

$$J = \int_{\Lambda}\left[\left(\sigma_{ij}\frac{\partial u_i}{\partial x_1} - W\delta_{1i}\right)\frac{\partial q}{\partial x_i} + \left(\alpha\sigma_{ii}\frac{\partial \overline{T}}{\partial x_1}\right)q_1\right]d\Lambda \quad (i,j = 1,2) \tag{10}$$

Where δ_{ij} is the Kronecker's delta, α is the coefficient of thermal expansion, $\overline{T}$ is the temperature net of zero-strain temperature and q is the crack extension vector, which is equal to zero at nodes along the path Γ, and it is equal to one at nodes inside Γ.

J-integral can be computed using the CINT command in Ansys just with structural elements, which do not support the concentration degree of freedom. Then, thermal strain is used to simulate chemical strain exploiting the similarities between the two phenomena, as explained previously in Eq. (8): α is replaced by $\Omega/3$, and temperature is replaced by lithium ion concentration in Eq. (10).

Finally, J-integral is equal to G when the path-independence property holds, according to LEFM theory. Then, mode-I SIF is directly

obtained from the J-integral as expressed in Eq. (11), neglecting mode-II and III as the corresponding fracture toughness (K_{IIc} and K_{IIIc}) are generally larger than the fracture toughness of mode-I (K_{Ic}).

$$K_I = \begin{cases} \sqrt{EJ_{MD}} & \text{plane stress} \\ \sqrt{\dfrac{EJ_{MD}}{(1-\nu^2)}} & \text{plane strain} \end{cases} \tag{11}$$

The minimum K_I value occurs in "plane stress" condition and the maximum in "plane strain", all the other cases fall in between. As the crack surfaces in the spherical particle are neither in plane stress nor plane strain, K_I is computed according to the plain strain, as it is the most severe condition.

2.2.4. Simulation strategy

Referring to Figure S3 of the Supplementary material, the simulation strategy adopted to compute fracture parameters in active material particles with pre-existent cracks is summarized as follows.

1. Lithium flux (J_{Li}) is computed using the P2D model according to the user-defined LIB operation.
2. Lithium flux (J_{Li}) is applied as boundary condition of the coupled mechanical-diffusive model of cracked particle implemented in Ansys. A particle with a pre-existent crack is modeled and the concentration distribution (c_s) is computed using the migration model in Ansys. The mutual influence between stress and concentration is captured, which is even more evident at the crack tip due to the stress singularity.
3. The concentration distribution ($\bar{c}_s$) is converted into temperature (T) and the thermal expansion coefficient is set equal to one-third of partial molar volume ($\alpha = \Omega/3$) thanks to the similarity between chemical and thermal strain (Eq. (8)).
4. Coupled field elements of the mechanical-diffusive FEM model are converted into their corresponding structural equivalent elements, keeping the same mesh pattern.
5. The equivalent temperature is mapped on the structural nodes of the FEM model including the crack surfaces.
6. A static fracture analysis is performed and the mode-I SIF is obtained by computing the J-integral through the CINT command of Ansys directly in the solution phase.

3. Results and discussion

Fracture in active material of LCO-graphite LIB is studied according to the multi-scale and multi-physics approach described in Section 2.2. Material properties and parameters used in the model are summarized in Table 2.

It is worth mentioning that the proposed modeling framework is general and applicable to a wide range of LIBs with different cell chemistry by choosing the proper material and geometric parameters, as well as by incorporating other kinetic and transport models as needed.

3.1. Validity of model assumptions

The validity of the assumptions of the electrochemical-fracture model presented in this work are discussed below.

- **Linear elastic active material.** Both LCO and graphite undergo small deformation during lithium insertion and extraction, then active material can be reasonably assumed linear elastic.
- **Spherical geometry with uniform size.** The shape and size of active material particles in the electrode have a certain statistical distribution. The geometry of graphite particles is close to a sphere, as confirmed by several SEM images [26,75], on the other hand, the geometry of LCO particles may be more irregular. However, an equivalent sphere with a mean radius representing the average particle distribution is widely accepted in literature.
- **Homogeneous isotropic active material.** LCO and graphite particles do not consist of several primary particles as other active materials, such as NMC and NCA, then the hypothesis of isotropy is reasonable. Furthermore, in the case of materials composed of primary particles (grains), the random distribution of the grains (which may have anisotropic characteristics) makes them not aligned, resulting in isotropic characteristics at the particle level. LCO and graphite are assumed to be homogeneous, neglecting phase transitions. This assumption is widely common in the literature and is supported by a recent work [76], showing good agreement between the cell deformation computed using the P2D model (with homogeneity assumptions) and the experimental measurements.
- **Crack influence on lithium flux.** Lithium flux distribution may be affected by superficial fractures which can increase the interface area with the electrolyte. Two effects may be considered: (a) the influence on the electrochemical behavior computed with P2D, because of the greater surface area; (b) the influence on the concentration distribution (and then stress) because of localized flux on the crack surfaces.
  Figure S4 in the Supplementary material shows that lithium flux computed with the P2D taking into account the additional crack surfaces (greater particle surface to volume ratio) is slightly lower with respect to the case without crack. The difference is less than 6% for LCO and 8% for graphite when $a/R = 0.5$, leading to an underestimation of SIF of 6% for LCO and 4% for graphite when cracked particles in the P2D model are considered.
  It is challenging to quantify the penetration of the electrolyte within the superficial cracks, and the value of the lithium flux over the crack surfaces in the fracture model. Anyway, two extreme cases exist: (1) the electrolyte cannot penetrate within the crack, then no lithium flux is applied on crack surfaces; (2) the electrolyte completely penetrates within the crack, then lithium flux is applied on the entire crack surfaces. Figure S5 in the Supplementary material shows that the localized lithium flux over the crack surfaces causes a steeper concentration gradient, resulting in higher stress. The higher stress results in an up to 11% overestimation of SIF when considering lithium flux over the entire crack surfaces.
  In conclusion, the effects (a) and (b) cancel each other, then P2D with uncracked particles and lithium flux applied just on the particle boundary is considered in the model.
- **Crack influence on lithium diffusion.** Fractures in the active material particles can change the pathways for lithium movement, both increasing or decreasing diffusion. This is because cracks surfaces, filled by the electrolyte, lead to new electrochemically active interfaces, which results in a higher apparent diffusion coefficient and a reduction of the pathway length for lithium ions [77,78]. On the other hand, internal cracks may interrupt the contact between active particles and conductive additives causing a loss in ionic diffusion [16].
  However, the crack influence on lithium diffusion pathways is neglected in this work because it is not completely understood and quantified in literature.

3.2. P2D model results

The electrochemical behavior of LCO-graphite LIB during charge and discharge is simulated with the P2D model using LIONSIMBA, considering crack-free active material. Starting from the full discharged state (0% SOC), the charge is performed by applying a positive constant current density until the battery reaches the cutover voltage (4.2 V), then the voltage is kept constant until the current drops below C/20. Similarly, the LIB is discharged starting from the fully charged state (100% SOC) and a negative constant current density is applied until the battery voltage drops below the cutoff voltage (3 V).

Table 2
P2D model parameters of the LCO-graphite LIB.

Parameter	Cathode (LCO) ($k = p$)	Separator ($k = s$)	Anode (Graphite) ($k = n$)
Geometry			
Thickness t	80 μm	50 μm	88 μm
Particle radius R_k	5 μm [65]	–	10 μm [66]
Active material fraction $\varepsilon_{s,k}$	0.7870 [67]	–	0.6860 [67]
Filler fraction $\epsilon_{f,k}$	0.028 [67]	–	0.056 [67]
Mechanical coupling			
Young's Modulus E_k	125 GPa [65]	–	15 GPa [68]
Poisson's ratio ν_k	0.3 GPa [65]	–	0.3 GPa [68]
Partial molar volume Ω_k	$-7.28 \cdot 10^{-7}$ $\frac{m^3}{mol}$ [69]	–	$4.253 \cdot 10^{-6}$ $\frac{m^3}{mol}$ [68]
Thermodynamic			
Minimum stoichiometric limit $\theta_k^{min} = \left(\frac{c_{s,k}}{c_{s,k}^{max}}\right)_{min}$	0.46 [67]	–	0.0224 [67]
Maximum stoichiometric limit $\theta_k^{max} = \left(\frac{c_{s,k}}{c_{s,k}^{max}}\right)_{max}$	0.9323 [67]	–	0.7557 [67]
Maximum concentration $c_{s,k}^{max}$	49934 $\frac{mol}{m^3}$ [70]	–	28700 $\frac{mol}{m^3}$ [70]
Kinetics			
Reaction rate $k_{e,k}$	$5 \cdot 10^{-12}$ $\frac{m^{2.5}}{mol^{0.5}s}$ [70]	–	$5 \cdot 10^{-12}$ $\frac{m^{2.5}}{mol^{0.5}s}$ [70]
Transport			
Solid-phase diffusivity $D_{s,k}$	$5.387 \cdot 10^{-15}$ $\frac{m^2}{s}$ [71]	–	$3.9 \cdot 10^{-14}$ $\frac{m^2}{s}$ [17]
Solid-phase conductivity $\sigma_{s,k}$	10 $\frac{S}{m}$ [71]	–	100 $\frac{S}{m}$ [17]
Electrolyte diffusivity $D_{e,k}$	$1.3 \cdot 10^{-10}$ $\frac{m^2}{s}$ [72]	$1.3 \cdot 10^{-10}$ $\frac{m^2}{s}$ [72]	$1.3 \cdot 10^{-10}$ $\frac{m^2}{s}$ [72]
Transference number t^+	0.363 [73]	0.363 [73]	0.363 [73]
Bruggemann coefficient *brugg*	1.5 [74]	1.5 [74]	1.5 [74]

Lithium flux, particle surface concentration, and maximum hoop stress within the electrode are reported in Fig. 2 for SOC equal to 25%, 50%, and 75% during 1C charge. The results for discharge are reported in Figure S6.

The P2D results demonstrate that lithiation and delithiation in LCO and graphite particles are not uniform. The lithium flux variation across LCO and graphite electrodes during delithiation is shown in Figs. 2a and S6b, respectively. Both LCO and graphite particles closer to the separator are subjected to the highest lithium flux at the beginning of delithiation. Then, the lithium flux peak decreases, moves along the electrode thickness and gets closer and closer to the current collector as long as the process proceeds. Finally, the lithium flux peak occurs closer to the current collector at the end of the delithiation. Similarly, the highest lithium flux occurs near the separator during lithiation, then it gradually decreases and moves towards the particles closer to the current collector, as shown in Fig. 2b and S6a. As a result, particles closer to the separator are emptied faster during delithiation, exhibiting lower surface concentration than the particles closer to the current collector, as shown in Figs. 2c and S6c. Vice versa during lithiation (Figs. 2d and S6d).

The non-homogeneous lithium flux influences the distribution of mechanical stress across the thickness of the electrodes. Figs. 3a, b and 3c,d show the maximum tensile hoop stress as a function of DOD and SOC during 1C discharge and charge respectively, considering particles located in three different spots across electrode thickness: near the separator, at the middle of the electrode, and near the current collector. The results show that particles located near the separator experience the highest hoop stress at the beginning of charge and discharge, being the most dangerous from the fracture point of view.

Based on the above discussion, active material particles at different locations along the electrode thickness may suffer a different level of fracture because the hoop stress changes along the electrode thickness during LIB operation. This result cannot be achieved when the full electrochemistry of the LIB is neglected, namely using a simplified algebraic expression for lithium flux or the SPM approach, as it has been done in some works in literature [52,53].

The effect of the mechanical-diffusive coupling on lithium flux, surface concentration, and maximum tensile hoop stress is also analyzed and shown in Figs. 2, S6, and 3. Lithium flux distributions obtained by considering and neglecting the mechanical-diffusive coupling are quite similar, as reported in Figs. 2a–b and S6 a–b. The similar trend is mainly attributed to the similar surface lithium concentrations obtained considering and neglecting the mechanical-diffusive coupling (2c–d and S6 c–d), which gives similar OCV and exchange current density values.

On the other hand, mechanical-diffusive coupling strongly affects DIS, as also demonstrated in previous authors' works [10,12]. This is because DIS and lithium transport are mutually coupled: the hydrostatic stress gradient always enhances lithium diffusion within particles, decreasing the concentration gradient, which decreases the stress in turn. Then, neglecting the mechanical-diffusion coupling gives higher concentration gradient and higher hoop stress, as it is also shown in Figures S7a–d and S8b–d, respectively.

The difference between the hoop stress values obtained using the coupled and uncoupled models increases when the concentration gradient increases, as shown in Fig. 3. The highest difference between coupled and uncoupled hoop stress values occurs in particles near the separator, because they experience the highest concentration gradient, on the other hand, a slight difference exists at the beginning and at the end of the charge and discharge, because of the more homogeneous concentration distribution.

3.3. Fracture model results

The results of the FEM fracture model are reported in this section, deepening the following topics:

- The influence of the mechanical-diffusive coupling.
- The crack growth stability.
- The influence of the operating conditions and geometric factors.

3.3.1. Influence of mechanical-diffusive coupling on fracture

Mechanics and lithium transport influence each other. The effect of this mutual interaction on the fracture behavior of active material particles is analyzed in this section.

The hydrostatic stress gradient always enhances lithium diffusion, leading to lithium accumulation or reduction at the crack tip, according to the sign of the partial molar volume (Ω). This concept is qualitatively explained in Fig. 4.

Referring to Fig. 4a, a central crack located in graphite particles undergoes tensile stress and may propagate during lithium insertion. On the other hand, a central crack located in LCO particles undergoes tensile stress during lithium extraction. The hydrostatic stress at the

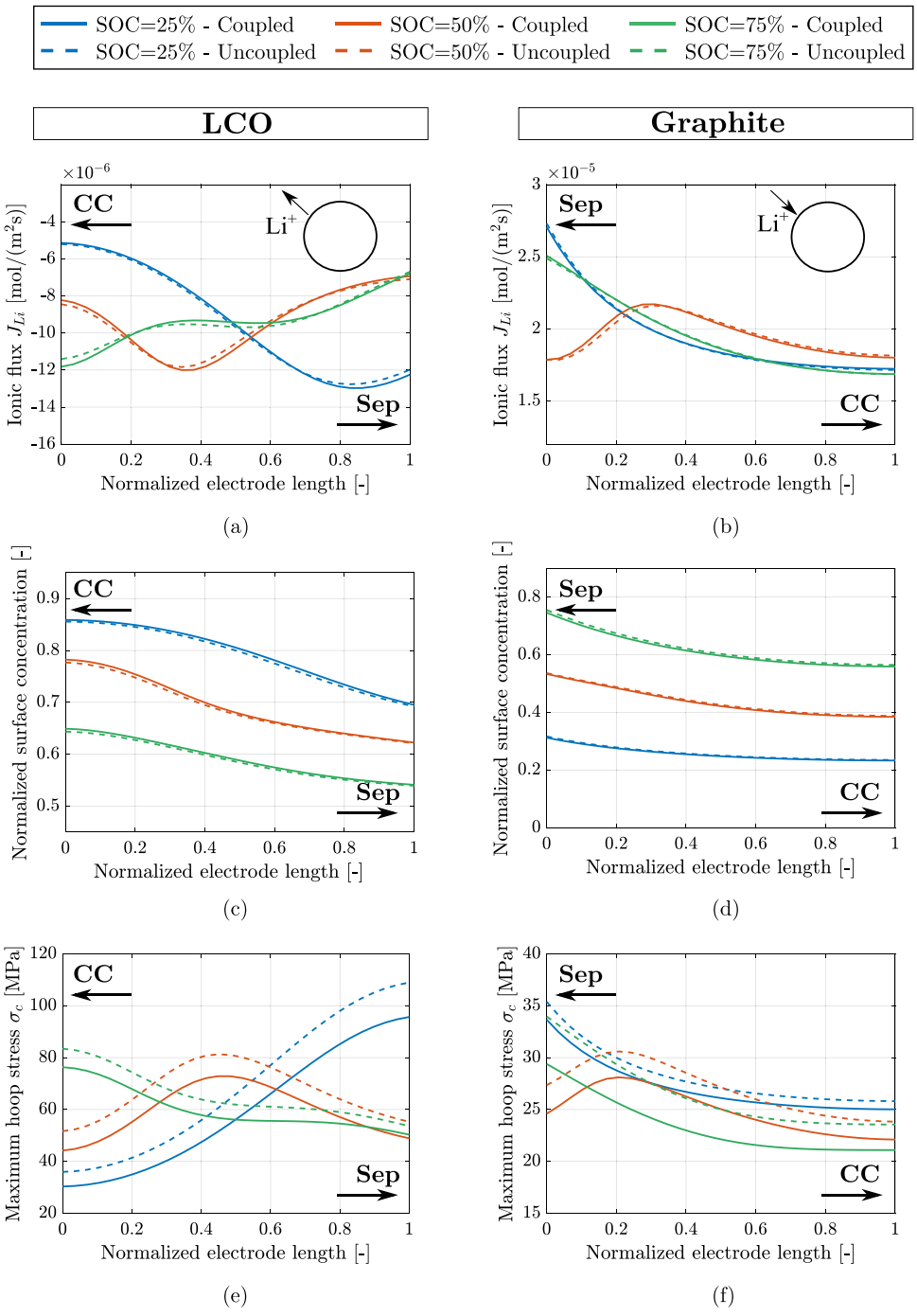

Fig. 2. P2D simulation results of LCO-graphite LIB charged at 1C rate for different SOC levels. Distribution of (a)–(b) ionic flux (J_{Li}), (c)–(d) superficial normalized concentration and (e)–(f) maximum tensile hoop stress (σ_c) on the particles surface across electrodes thickness.

crack tip (referred to as point 1 in Fig. 4a) is significantly higher than in neighboring areas, i.e. a point located at a distance dr from the crack tip (referred to as point 2 in Fig. 4a), according to the LEFM theory. Then, the hydrostatic stress gradient ($\frac{\partial \sigma_h}{\partial r}$) is always negative in the region near the crack tip.

The contribution to diffusion of the hydrostatic stress gradient ($-\Omega \frac{\partial \sigma_h}{\partial r}$) is concordant with the sign of the lithium flux, then it concurs to the incoming flux in the case of graphite (positive partial molar volume), and to the outgoing flux in the case of LCO (negative partial molar volume). As a result, lithium ions are driven to the crack tip and accumulate during lithium insertion in graphite particles, leading to higher lithium concentration in a small localized area. On the other hand, lithium ions are pushed away from the crack tip during lithium extraction in LCO particles, resulting in lower concentration than in neighboring areas.

This analysis is also valid for lithium extraction from graphite particles and lithium insertion in LCO particles with a superficial crack, as explained in Fig. 4b. In this case, the hydrostatic stress gradient ($\frac{\partial \sigma_h}{\partial r}$) is positive, then the contribution of the hydrostatic stress gradient ($-\Omega \frac{\partial \sigma_h}{\partial r}$) is discordant with the sign of lithium flux. Then lithium is pushed toward the crack tip in graphite particle during extraction and away from the crack tip in LCO particle during insertion.

Although the crack affects lithium concentration in graphite and LCO particles according to the sign of the partial molar volume, the respective change in lithium concentration has the same effect on the

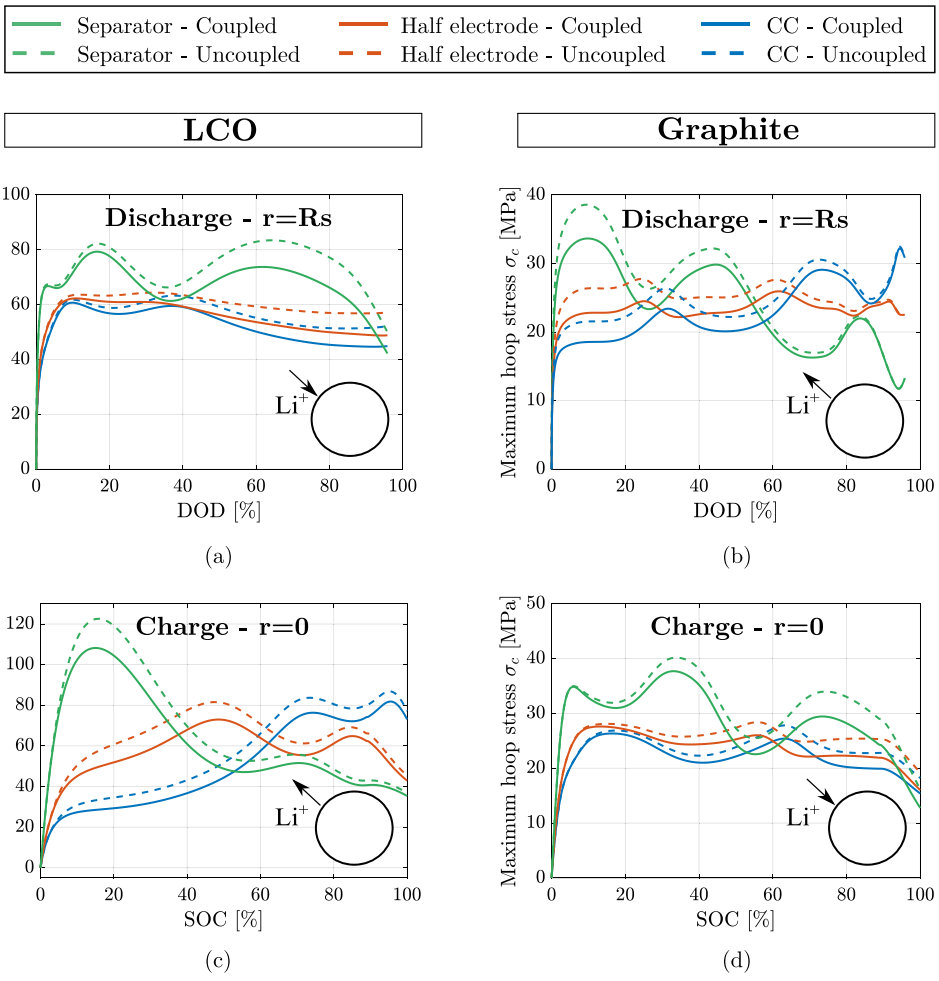

Fig. 3. Maximum tensile hoop stress as a function of DOD and SOC in particles at three spots across the electrode thickness: near the separator, at the middle of the electrode, and near the current collector. (a) LCO and (b) graphite particles during 1C discharge. (c) LCO and (d) graphite particles during 1C charge. Dashed lines refer to the uncoupled model and solid lines refer to the coupled model.

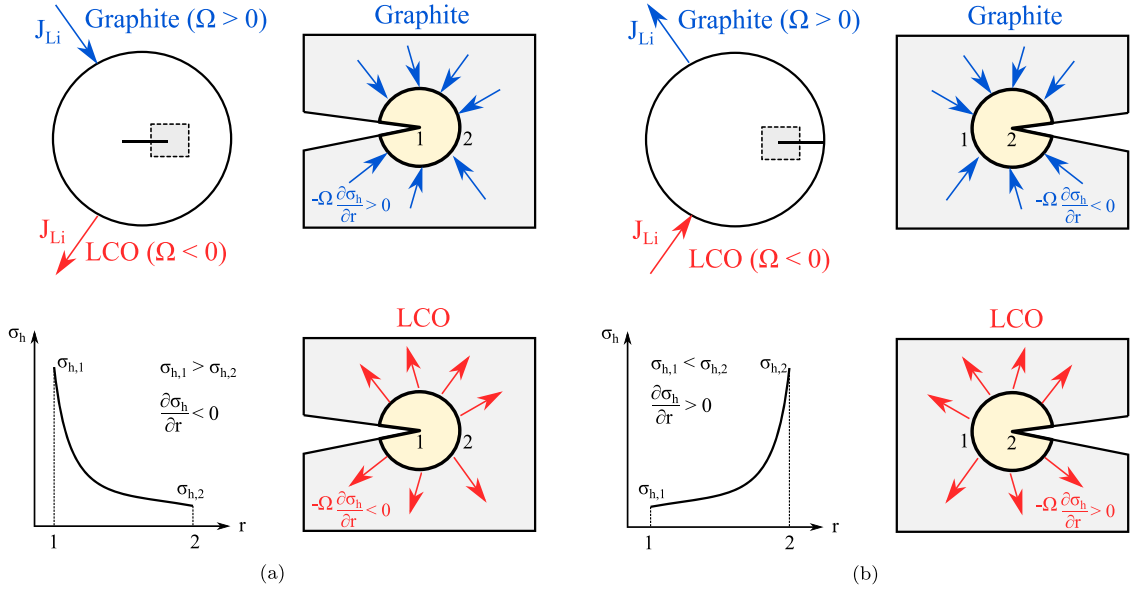

Fig. 4. Effect of mechanical-diffusive coupling on lithium diffusion near the crack tip region in graphite and LCO particle with (a) central crack during charge and (b) superficial crack during discharge. The lithium flux is $J_{Li} = -D\left(\frac{\partial c}{\partial r} - \Omega \frac{\partial \sigma_h}{\partial r} \frac{c}{R_g T}\right)$ and is positive if outgoing.

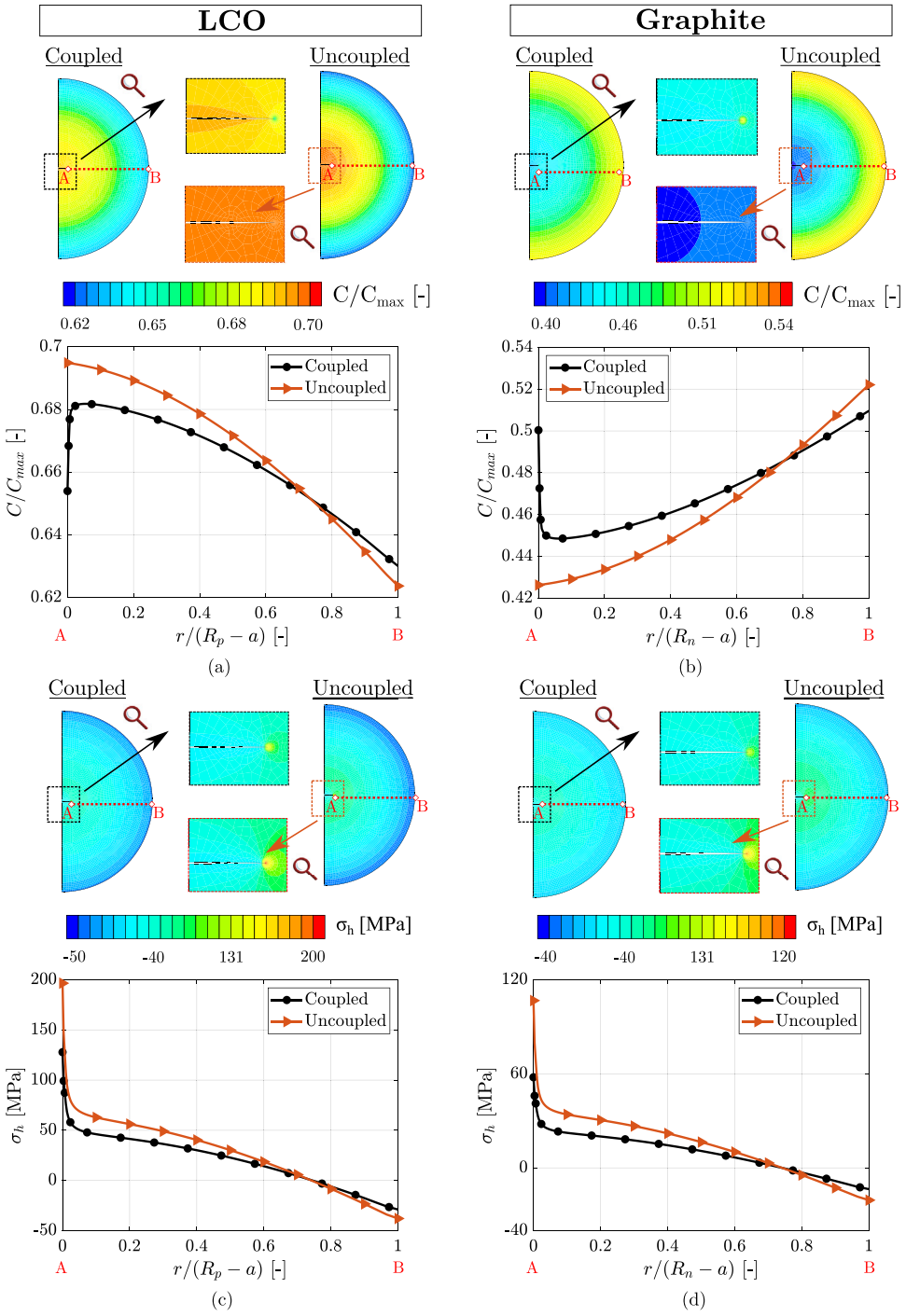

Fig. 5. Concentration and hydrostatic stress distribution in LCO (a)–(c) and graphite (b)–(d) particles obtained with coupled and uncoupled models. Results are obtained for 1C charge at SOC 50%. The radial distribution of concentration and hydrostatic stress along the A–B path are plotted in the diagrams beneath.

stress at the crack tip. Indeed, the extra lithium concentration driven by the higher tensile stress at the crack tip in graphite particle causes the area around the crack tip to expand (Ω is positive). The total deformation keeps constant (left-hand side of Eq. (1)a) because the lithium ions quantity which is inserted or extracted from the particle keeps constant [13,79], then the rise of the volumetric expansion caused by lithium accumulation (second term in the right-hand side of Eq. (1)a), counterbalances the elastic deformation (first term of the right-hand side of Eq. (1)a), leading to a reduction in the overall tensile stress in the crack region. Similarly, the concentration drop at the crack tip of LCO particles causes the material near the crack tip to expand because of the negative partial molar volume, decreasing the elastic component of deformation, and stress in turn.

Fig. 5 shows the concentration and hydrostatic stress distributions in LCO and graphite particles during 1C charge at SOC 50%. Both the particles have a central pre-existent crack ($a/R = 0.1$) and are located close to the separator.

Lithium ions are driven (graphite) or pushed away (LCO) from the crack tip when the mechanical-diffusive coupling is taken into account. Then, lithium concentration at the crack tip is higher in graphite

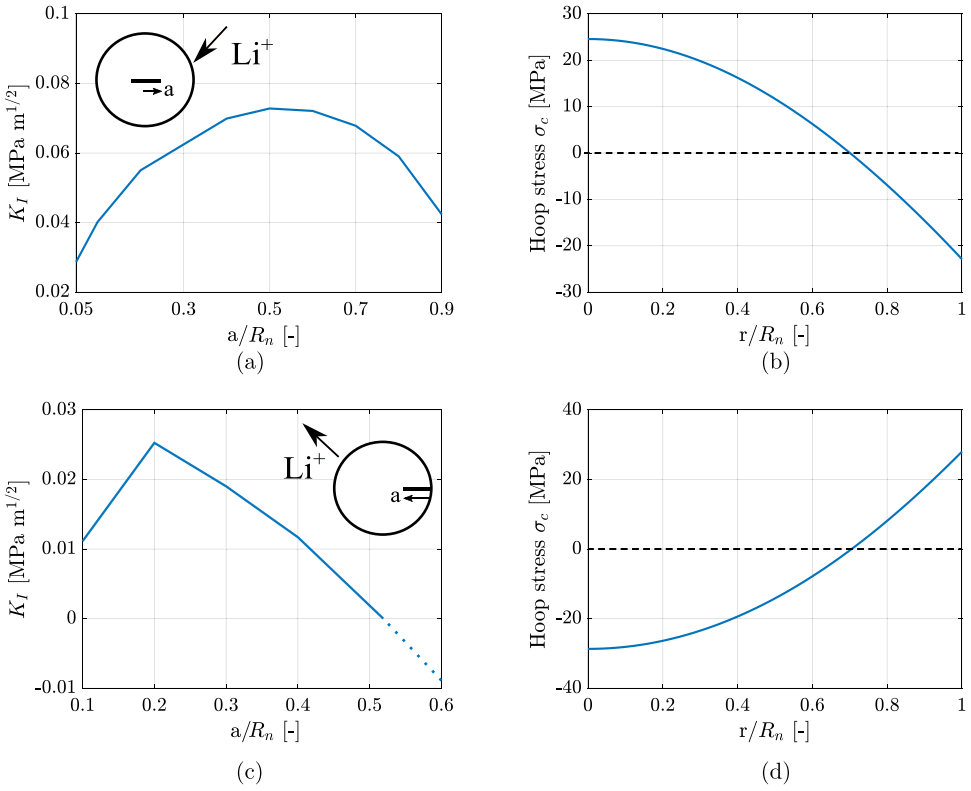

Fig. 6. Assessment of crack growth stability in graphite particles near the separator. K_I as a function of normalized crack length (a/R_n) during (a) charge and (c) discharge at 1C. Hoop stress distribution along the normalized radial coordinate r/R_n during (b) charge and (d) discharge at 1C. The dotted line shows the where the hoop stress changes sign.

particles and lower in LCO particles, as depicted in the enlarged concentration profile in the upper part of Figs. 5a and b respectively. The concentration distribution has a spherical symmetry and is not influenced by the stress singularity away from the crack region. On the other hand, lithium is just driven by the concentration gradient when the mechanical-diffusive coupling is neglected and lithium concentration is not influenced by the crack.

The highest difference between concentration values computed considering or neglecting the mechanical-diffusive coupling occurs at the crack tip and is equal to 6% for LCO and 17% for graphite particles. Then, the hydrostatic stress relaxes up to 36% in LCO and 43% in graphite particles (Figs. 5c and d), due to the balance between elastic and chemical deformation, as explained before.

Figure S9 shows the concentration and hydrostatic stress distributions in LCO and graphite particles during 1C discharge at DOD 50%. Both particles are located near the separator and have a superficial crack ($a/R = 0.1$). The results are similar to the ones obtained during the charge. Indeed, lithium diffusion is not affected by the stress singularity when the mechanical-diffusive coupling is neglected and there is no jump in lithium concentration at the crack tip, on the other hand, the mechanical-diffusive coupling increases and decreases the concentration at the crack tip in graphite and LCO particles, respectively (Figures S9a and b).

The relaxation of the hydrostatic tensile stress caused by the change in the local concentration at the crack tip during discharge is up to 29% and 30% for LCO and graphite particles, respectively (Figures S9c and d).

Based on the above discussion, the driving force for crack growth is expected to decrease when the mechanical-diffusive coupling is considered due to the decrease in the stress field at the crack tip, as it will be further discussed in Section 3.3.4.

3.3.2. Path-independence of the mechanical-diffusive J-integral

The mode-I SIF (K_I) is computed with the mechanical-diffusive J-integral (J_{MD}) once lithium concentration distribution is obtained, exploiting the thermal analogy as previously explained in Section 2.2.

The path-independence property of the J_{MD} is verified by checking its convergence over different independent contours, characterized by an increasing distance from the crack region.

Figures S10a–b show the J_{MD} values computed over eight contours for LCO and graphite particles with central crack during charge (2D model). The results show that the J_{MD} converges to a constant value after the fifth contour, meaning that it is path-independent.

Figures S10c, d show the J_{MD} distribution along the front of the superficial crack in LCO and graphite particles during discharge (3D model). The J_{MD} distribution is not uniform along the crack front in the 3D model and it has the highest values on the particle surface, i.e. where the hoop stress is maximum. Furthermore, the matching of the J-integral values computed from the third contour demonstrates the path independence.

3.3.3. Stability of crack growth

Generally speaking, crack propagation can be classified as stable or unstable. Crack growth stability depends on the evolution of SIF with respect to the crack length (a), on the geometry, loading, and material behavior. Unstable crack growth should be avoided to prevent rapid fracture of active material particles and fast LIB degradation.

When static loading is considered, cracks propagate when SIF overcomes the fracture toughness ($K > K_c$). Furthermore, the propagation may be unstable if SIF increases with the crack length ($\frac{\partial K}{\partial a} > 0$), otherwise it is stable [80].

Then, the variation of K_I with respect to the crack length a during charge/discharge is computed to assess the crack growth stability. Figs. 6a,c shows the maximum K_I occurring during LIB charge and discharge at 1C as a function of the normalized crack length (a/R),

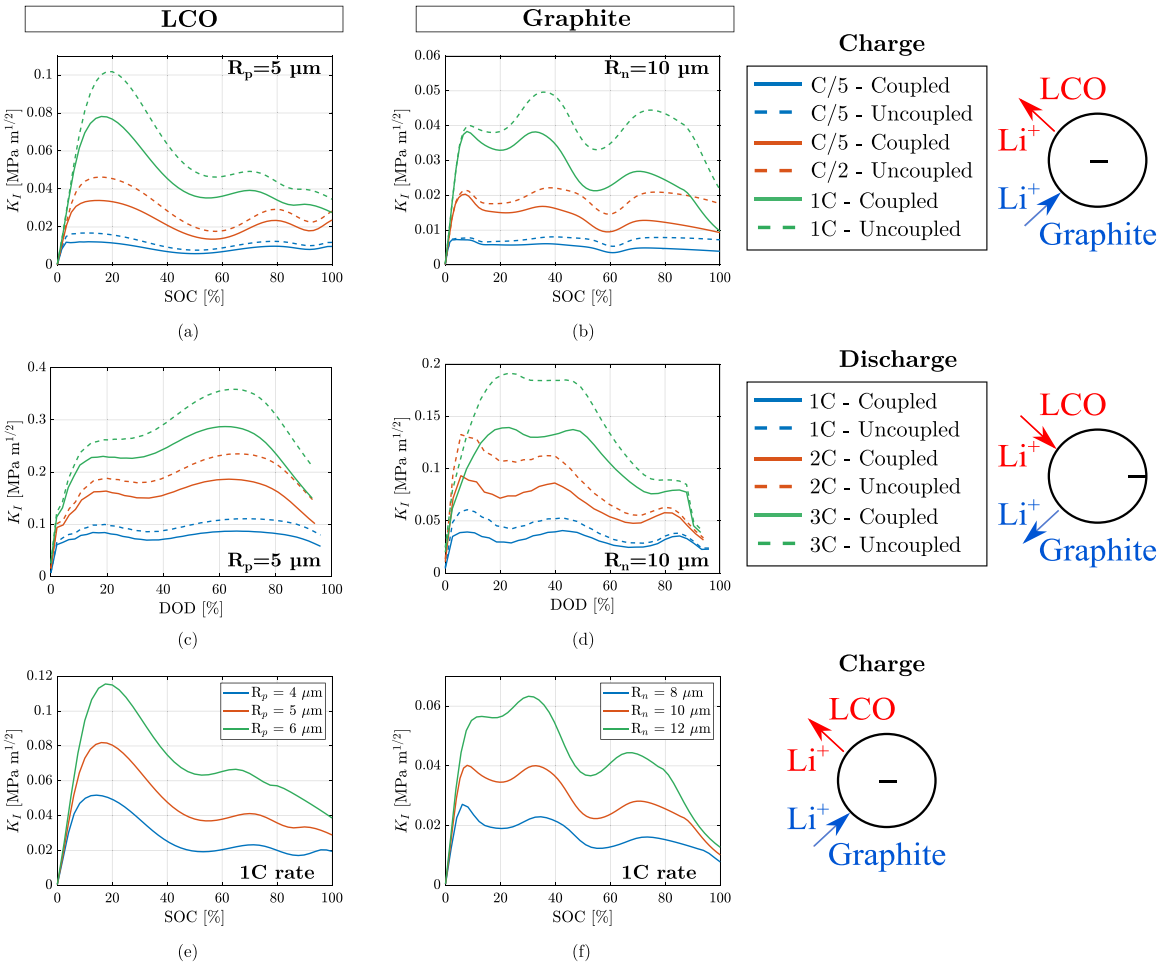

Fig. 7. Influence of current rates and particle radius on K_I. K_I as a function of SOC during charge at different C-rates: (a) LCO and (b) graphite particles with central crack. K_I as a function of DOD during discharge at different C-rates: (c) LCO and (d) graphite particles with superficial crack. K_I as a function of SOC during 1C charge at different particle radii: (e) LCO and (f) graphite particles with central crack. Dashed lines refer to the uncoupled model and solid lines refer to the coupled model.

considering graphite particles with central and superficial crack, respectively. The particles are located near the separator, which is the most stressed region as previously reported in Section 3.2. Furthermore, K_I values computed using the 3D model refer to the inner point along the crack front.

Referring to the case of the particle with a central crack during lithium insertion (Figs. 6a, b), the results show that a longer initial crack leads to greater K_I as long as the normalized crack length is lower than $a/R = 0.5$, then the increase in crack length leads to a decrease in K_I. Similarly, considering the particle with a superficial crack during lithium extraction (Figs. 6c, d), K_I increases as long as the crack tip position is close enough to the surface, i.e. a/R is lower than 0.2, then K_I decreases as the crack tip gets closer to the particle center.

The K_I variation with respect to the normalized crack length in LCO particle has the same trend and is reported in Figure S11 of the Supplementary material for the sake of completeness.

The K_I variation reported in Figs. 6 and S11 can be explained as follows. Remembering that the generic expression of mode-I SIF is equal to $K_I = \sigma_c Y \sqrt{a}$, (where Y is the geometric factor), K_I increases if the crack length (a) and the hoop stress (σ_c) increase. The value of the hoop stress (σ_c) is not constant within the particle but it changes according to the radial coordinate, namely, it decreases and becomes compressive going from the particle core to the surface during charge (Fig. 6b and S11b) and going from the particle surface to the core during discharge (Fig. 6d and S11d). Then, longer central cracks experience lower hoop stress than smaller cracks as the crack tip of longer cracks is closer to the surface. The same happens in the case of superficial cracks, namely the crack tip of longer superficial cracks experiences lower hoop stress as it gets closer to the particle center. As a result, the increase in the crack length increases the K_I as long as it balances the decrease in the hoop stress.

Considering that unstable crack growth occurs when the slope of K with respect to a is positive ($\frac{\partial K}{\partial a} > 0$), unstable growth is likely when SIF overcomes the fracture toughness, according to Figs. 6 and S11. Indeed, $\frac{\partial K}{\partial a}$ becomes negative beyond $a/R = 0.5$ in insertion, which is a non-physical initial crack length, and $\frac{\partial K}{\partial a}$ becomes negative beyond $a/R_n = 0.2$ in extraction, which is still a very long initial crack size.

However, it is very unlikely that SIF can overcome the fracture toughness and the case is limited to extremely high current rates. Indeed, fracture toughness is 0.79 MPa $m^{1/2}$ for graphite [81] and ranges between 0.26 and 1.04 MPa $m^{1/2}$ for LCO [82]. Then, significant crack propagation in a single cycle is unlikely, but fatigue due to repeated charge and discharge cycles is the main cause of crack propagation at practical current rates.

3.3.4. Influence of the operating condition and geometric factors

Fig. 7 shows the mode-I SIF (K_I) as a function of SOC during LIB charge (Figs. 7a–b) and discharge (Figs. 7c–d) at different C-rates. LCO and graphite particles with internal (during charge) and superficial (during discharge) cracks of $a/R = 0.1$ are considered. Particles located near the separator are analyzed, being the most severe condition from the fracture point of view, as characterized by higher stress according to the results of Section 3.2. Furthermore, K_I values computed using the 3D model refer to the inner point along the crack front.

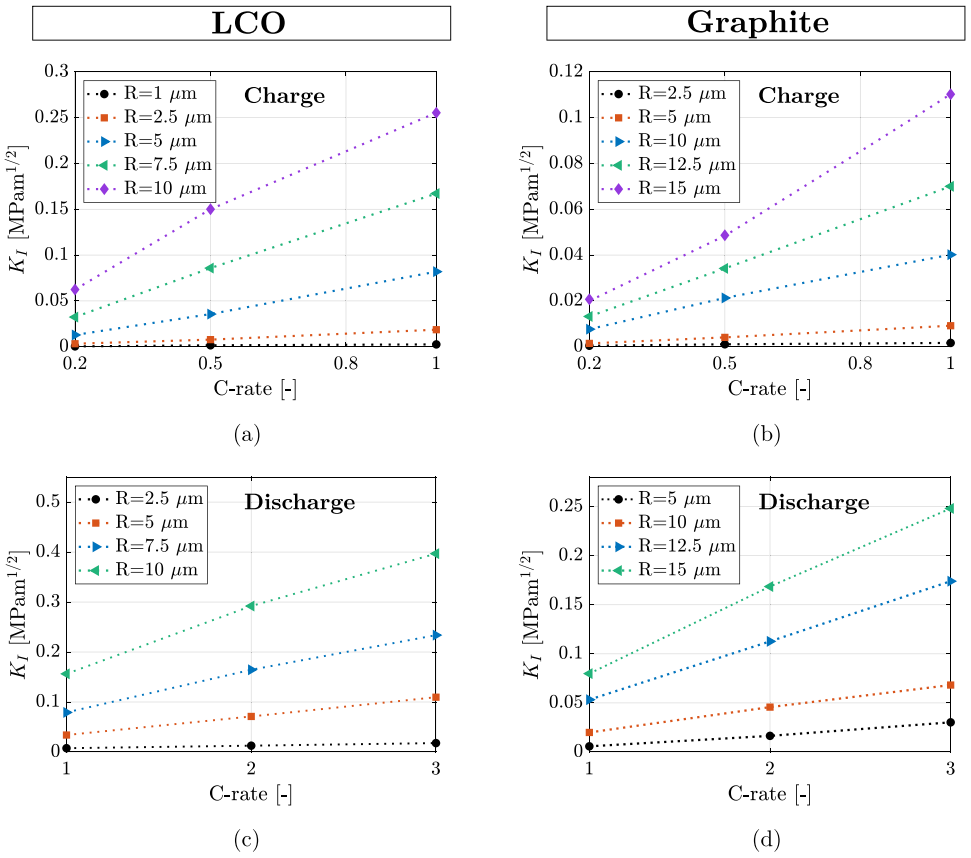

Fig. 8. K_I in LCO and graphite particles near the separator interface as a function of particle radius and current rate. (a) LCO and (b) graphite during charge; (c) LCO and (d) graphite during discharge.

The results show that K_I is not constant during LIB charge and discharge, following the same trend of the hoop stress (Fig. 3). The C-rate affects the value of K_I, as higher C-rate causes higher concentration gradients within active material particles, resulting in higher stress, then higher K_I. This trend is also confirmed by some experimental [27,83,84] and numerical [85] works, showing that higher C-rates increase fracture and accelerate the LIB performance decay.

Fig. 7 also shows the comparison between K_I values obtained considering and neglecting the mechanical-diffusive coupling. The results demonstrate that K_I is overestimated when the mechanical-diffusive coupling is neglected. This is because the uncoupled model predicts higher hoop stress due to the higher concentration gradient, as well as it does not capture the decrease in the hoop stress near the crack tip due to the redistribution of lithium ions. For example, K_I is overestimated up to 31% and 78% in LCO and graphite particles during 1C charge, respectively. Furthermore, the overestimation of K_I is not constant throughout the SOC (or DOD) range: a slight difference between coupled and uncoupled results exists at the beginning of charge (or discharge) due to the lower concentration gradient, then the difference increases at higher SOC (or DOD).

The variation of K_I in LCO and graphite particles with different radii during 1C charge is reported in Figs. 7e and f, respectively. The results show that K_I increases as the particle radius increases, because the concentration gradient, as well as the hoop stress, increase with increasing the particle radius. Then, larger particles are more detrimental from the fracture point of view, which is in agreement with some experimental works [86] (https://doi.org/10.1002/batt.202300203).

Fig. 8 shows the maximum K_I during charge and discharge in LCO and graphite particles located near the separator, as a function of the particle radius and current rate. The range of particle radii is based on the minimum and maximum values found in the literature to quantify the influence of particle size and current rate on fracture, aiming to provide practical suggestions for the electrode design.

The results show that K_I has a linear trend with respect to the current rate. Furthermore, particle size has a significant detrimental effect on fracture. This result underlines how the current rate and particle size have a significant impact on fracture and can play a strategic role in the electrode design.

Considering that the maximum C-rate is a LIB requirement established by the manufacturer, it should be kept as low as possible during operation to limit fracture. From the electrode design point of view, given the maximum current rate, the particle size should be chosen accordingly to achieve the admitted level of fracture. Furthermore, particle size should be reduced especially near the separator as this is the most stressed region, although it could be challenging from the manufacturing point of view.

However, it is important to point out that electrode with smaller active material particles result in LIB with lower tap density and energy density. Furthermore the electrode would require more supporting materials (conductive carbon and binder) and would result in a higher manufacturing cost [87]. In addition, smaller particles are more prone to side-reaction with the electrolyte due to the increased surface area [88]. Then, the reduction of particle size may improve the life performance of LIBs because it decreases fracture, but a very small particle size could be negative from the cost and the electrochemical performance point of view. As a consequence, the particle size has to be chosen according to the different LIBs applications and the available manufacturing process in order to have LIBs with the best electrochemical performance and the longest cycle life.

4. Conclusion

A multi-physics and multi-scale model is presented in this work to study fracture in electrode active material of LIBs. The model is

Table A.3
Governing equations of the P2D model for LIBs [63]. Subscripts n, p, and s stand for the anode, separator and cathode, respectively, whereas subscripts a and z stand for the positive and negative current collector, respectively.

Description	Governing equations		Boundary conditions
	Active material particles, $i \in \{p,n\}$		
Mass conservation	$\frac{\partial c_{s,k}}{\partial t} = \nabla \cdot \left[D_{s,i}^{\text{eff}} \left(\frac{\partial c_{s,k}}{\partial r} - \frac{\Omega_k c_{s,k}}{RT} \frac{\partial \sigma_{h,i}}{\partial r} \right) \right]$	*(A.1)*	$D_{s,i}^{\text{eff}} \left(\frac{\partial c_{s,k}}{\partial r} - \frac{\Omega_k c_{s,k}}{RT} \frac{\partial \sigma_{h,i}}{\partial r} \right)\Big\|_{r=0} = 0,$ $D_{s,i}^{\text{eff}} \left(\frac{\partial c_{s,k}}{\partial r} c_{s,k} - \frac{\Omega_k c_{s,k}}{RT} \frac{\partial \sigma_{h,i}}{\partial r} \right)\Big\|_{r=R_{p,i}} = -J_{Li,k}$
Charge conservation	$\frac{\partial}{\partial x} \left(\sigma_{s,i}^{\text{eff}} \frac{\partial \Phi_{s,i}}{\partial x} \right) = a_{s,k} J_{Li,k}$	*(A.2)*	$\sigma_{s,i}^{\text{eff}} \frac{\partial \Phi_{s,i}}{\partial x})\Big\|_{x=0,\, l_p+l_s+l_n} = I_i,$ $\sigma_{s,i}^{\text{eff}} \frac{\partial \Phi_{s,i}}{\partial x})\Big\|_{x=l_p,\, l_p+l_s} = 0$
	Electrolyte, $i \in \{p,s,n\}$		
Mass conservation	$\epsilon_{e,i} \frac{\partial c_{e,i}}{\partial t} = \frac{\partial}{\partial x} \left(D_{e,i}^{\text{eff}} \frac{\partial c_{e,i}}{\partial x} \right) + a_{s,k}(1-t_+) J_{Li,k}$	*(A.3)*	$\frac{\partial c_{e,i}}{\partial x}\Big\|_{x=0,\, l_p+l_s+l_n} = 0$
Charge conservation	$\frac{\partial}{\partial x} \left[\kappa_{e,i}^{\text{eff}} \left(\frac{\partial \Phi_{e,i}}{\partial x} - \frac{2(1-t^+) R_g T}{F} \frac{\partial \ln(c_{e,i})}{\partial x} \right) \right] = -a_{s,k} J_{Li,k}$	*(A.4)*	$\frac{\partial \Phi_{e,i}}{\partial x}\Big\|_{x=0,\, l_p+l_s+l_n} = 0,$ $\Phi_{e,i}\Big\|_{x=0,\, l_p+l_s+l_n} = 0$
	Reaction kinetics		
Butler-Volmer	$J_{Li,k} = \begin{cases} 2 \frac{i_{0,i}}{F} \sinh \frac{0.5F}{RT} \eta_i & i \in \{p,n\} \\ 0 & i = s \end{cases}$	*(A.5)*	–
Exchange current	$i_{0,i} = F k_i^{\text{eff}} \left[c_{e,i} c_{s,i}^{\text{surf}} \left(c_{s,i}^{\max} - c_{s,i}^{\text{surf}} \right) \right]^{0.5}$	*(A.7)*	–
Overpotential	$\eta_i(x,t) = \Phi_{s,i}(x,t) - \Phi_{e,i}(x,t) - U_i, i \in \{p,s\}$	*(A.7)*	–
	Thermal equations		
Energy balance (active material) $i \in \{p,n\}$	$\rho_i C_{p,i} \frac{\partial T}{\partial t} = \frac{\partial}{\partial x} \left[\lambda_i \frac{\partial T}{\partial x} \right] + Q_{ohm} + Q_{rxn} + Q_{rev}$	*(A.8)*	$-\lambda_z \frac{\partial T}{\partial x}\Big\|_{x=0^-} = -\lambda_p \frac{\partial T}{\partial x}\Big\|_{x=0^+}$ $-\lambda_n \frac{\partial T}{\partial x}\Big\|_{x=l_n^-} = -\lambda_z \frac{\partial T}{\partial x}\Big\|_{x=l_n^+}$
Energy balance (separator) $i = s$	$\rho_i C_{p,i} \frac{\partial T}{\partial t} = \frac{\partial}{\partial x} \left[\lambda_i \frac{\partial T}{\partial x} \right] + Q_{ohm}$	*(A.9)*	$-\lambda_p \frac{\partial T}{\partial x}\Big\|_{x=l_p^-} = -\lambda_s \frac{\partial T}{\partial x}\Big\|_{x=l_p^+}$ $-\lambda_s \frac{\partial T}{\partial x}\Big\|_{x=l_s^-} = -\lambda_n \frac{\partial T}{\partial x}\Big\|_{x=l_s^+}$
Energy balance (current collectors) $i \in \{a,z\}$	$\rho_i C_{p,i} \frac{\partial T}{\partial t} = \frac{\partial}{\partial x} \left[\lambda_i \frac{\partial T}{\partial x} \right] + \frac{I_i^2}{\sigma_{s,i}^{\text{eff}}}$	*(A.10)*	$-\lambda_a \frac{\partial T}{\partial x}\Big\|_{x=0} = h\left(T_{ref} - T\right)$ $-\lambda_z \frac{\partial T}{\partial x}\Big\|_{x=l_p+l_s+l_n} = h\left(T - T_{ref}\right)$
Ohmic heat (active material) $i \in \{p,n\}$	$Q_{ohm} = \sigma_{s,i}^{\text{eff}} \left(\frac{\partial \Phi_{s,i}}{\partial x} \right)^2 + \kappa_{e,i}^{\text{eff}} \left(\frac{\partial \Phi_{e,i}}{\partial x} \right)^2 + \frac{2\kappa_{e,i}^{\text{eff}} RT}{F}(1-t_+) \frac{\partial \ln c_{e,i}}{\partial x} \frac{\partial \Phi_{e,i}}{\partial x}$	*(A.11)*	–
Ohmic heat (separator) $i = s$	$Q_{ohm} = \kappa_{e,i}^{\text{eff}} \left(\frac{\partial \Phi_{e,i}}{\partial x} \right)^2 + \frac{2\kappa_{e,i}^{\text{eff}} RT}{F}(1-t_+) \frac{\partial \ln c_{e,i}}{\partial x} \frac{\partial \Phi_{e,i}}{\partial x}$	*(A.12)*	–
Reaction heat (active material) $i \in \{p,n\}$	$Q_{rxn} = a_{s,k} J_{Li,k} \eta_i$	*(A.13)*	–
Reversible heat (active material) $i \in \{p,n\}$	$Q_{rev} = a_{s,k} J_{Li,k} T \frac{\partial U_i}{\partial T}\Big\|_{T_{ref}}$	*(A.14)*	–

general and applicable to LIBs with different electrode materials by choosing the proper material and geometric parameters. LCO-graphite LIB is chosen as case study in this work.

The full LIB electrochemistry is modeled according to the P2D model to compute the lithium flux on particles as a function of the electrode thickness, later used as the boundary condition of the coupled mechanical-diffusive FEM fracture model. This allows computing the fracture behavior due to the real LIB usage.

The mechanical-diffusive coupling considered in the model causes the reduction of the hoop stress due to the lower concentration gradient in the particle and the redistribution of lithium ions at the crack tip caused by the higher stress near the crack tip. The results demonstrate that the mode-I SIF is overestimated up to 50% when the mechanical-diffusive coupling is neglected.

The propagation of the crack due to static loading and its stability is studied, demonstrating that the propagation due to a single (de)lithiation cycle is very unlikely, as SIF does not overcome the fracture toughness at practical current rates, but when it occurs (limited to extremely high current rates), the propagation is likely to be unstable. Fatigue because of repeated charge/discharge cycles occurring when SIF is lower than the fracture toughness is the most likely cause of crack propagation.

Finally, the effect of current rate and particle size on SIF are quantified. Both have a significant impact on SIF and on the likelihood to cause fracture, then current rate and particle size could be ideally kept as low as possible. Assuming that the current rate is a LIB requirement, particle size can be designed accordingly in order to limit fracture and improve LIB life. In general, a trade-off on particle size has to be made in the electrode design, as smaller particles improve the fracture behavior but worsen the electrochemical performance and increase the manufacturing cost.

CRediT authorship contribution statement

Francesca Pistorio: Conceptualization, Methodology, Software, Validation, Writing – original draft, Visualization. **Davide Clerici:** Conceptualization, Methodology, Writing – review & editing. **Francesco Mocera:** Conceptualization, Writing – review & editing, Supervision. **Aurelio Somà:** Conceptualization, Writing – review & editing, Supervision, Project administration.

Table A.4
Thermal dependence of Open Circuit Voltage (OCV) [63]. Subscript p and n refers to cathode and anode, respectively.

Open circuit potential	
$U_i = U_{i,ref} + (T - T_{ref}) \frac{\partial U_i}{\partial T}\Big\|_{T_{ref}} \quad i \in \{p, n\}$	(A.15)
$U_{p,ref} = 4.04596 + \exp(-42.30027 \cdot \theta_p + 16.56714) - 0.048 \cdot (50.01833 \cdot \theta_p - 26.48897) + -0.05447(18.99678 \cdot \theta_p - 12.32362) - \exp(78.240895 \cdot \theta_p - 78.68074)$	(A.16)
$U_{n,ref} = 0.124 + 1.5\exp(-150 \cdot \theta_n) + 0.0155\tanh\left(\frac{\theta_n - 0.105}{0.029}\right) - 0.011\tanh\left(\frac{\theta_n - 0.124}{0.0226}\right) + -0.102\tanh\left(\frac{\theta_n - 0.194}{0.142}\right) + 0.0347\tanh\left(\frac{\theta_n - 0.286}{0.083}\right) - 0.0147\tanh\left(\frac{\theta_n - 0.5}{0.034}\right) + -0.0045\tanh\left(\frac{\theta_n - 0.9}{0.119}\right) - 0.022\tanh\left(\frac{\theta_n - 0.98}{0.0164}\right) - 0.035\tanh\left(\frac{\theta_n - 0.99}{0.05}\right)$	(A.17)
$\frac{\partial U_p}{\partial T}\Big\|_{T_{ref}} = -0.001\left(\frac{0.199521039 - 0.928373822 \cdot \theta_p + 1.364550689000003 \cdot \theta_p^2 - 0.6115448939999998 \cdot \theta_p^3)}{1 - 5.661479886999997 \cdot \theta_p + 11.47636191 \cdot \theta_p^2 - 9.82431213599998 * theta_p^3 + 3.048755063 \cdot \theta_p^4}\right)$	(A.18)
$\frac{\partial U_n}{\partial T}\Big\|_{T_{ref}} = \frac{0.001\left(\begin{array}{c}0.005269056 + 3.299265709\theta_n - 91.79325798\theta_n^2 + 1004.911008\theta_n^3 - 5812.278127\theta_n^4 + \\ 19329.7549\theta_n^5 - 37147.8947\theta_n^6 + 38379.18127\theta_n^7 - 16515.05308\theta_n^8\end{array}\right)}{\left(\begin{array}{c}1 - 48.09287227\theta_n + 1017.234804\theta_n^2 - 10481.80419\theta_n^3 + 59431.3\theta_n^4 - \\ 195881.6488\theta_n^5 + 374577.3152\theta_n^6 - 385821.1607\theta_n^7 + 165705.8597\theta_n^7\end{array}\right)}$	(A.19)
$\theta_p = \frac{c_{s,p}}{c_{s,p}^{\max}}$	(A.20)
$\theta_n = \frac{c_{s,n}}{c_{s,n}^{\max}}$	(A.21)

Table A.5
Effective P2D model coefficients with correction for thermal effects [63]. Subscripts p, s, n stand for cathode, separator and anode, respectively.

Coefficients		
$D_{s,i}^{\text{eff}} = D_{s,k}\exp\frac{-E_a}{R}\left(\frac{1}{T} - \frac{1}{T_{ref}}\right)$	$i \in \{p, n\}$	(A.22)
$\sigma_{s,i}^{\text{eff}} = \sigma_{s,k}(1-\varepsilon_{s,i}-\varepsilon_{f,i})$	$i \in \{p, n\}$	(A.23)
$D_{e,i}^{\text{eff}} = \varepsilon_{s,i}^{brugg_i} \cdot 10^{-4} \cdot 10^{-4.43 - \frac{54}{T-229-5\cdot10^{-3}c_e} - 0.22\cdot10^{-3}c_e}$	$i \in \{p, s, n\}$	(A.24)
$\kappa_{e,i}^{\text{eff}} = \varepsilon_{s,i}^{brugg_i} \cdot 10^{-4} \cdot c_e\left(\begin{array}{c}-10.5 + 0.668\cdot10-3\cdot c_e + 0.494\cdot10^{-6}c_e^2 \\ (0.074 - 1.78\cdot10^{-5}c_e - 8.86\cdot10^{-10}c_e^2)T + \\ (-6.96\cdot10^{-5} + 2.8\cdot10^{-8}c_e)T^2\end{array}\right)^2$	$i \in \{p, s, n\}$	(A.25)
$k_i^{\text{eff}} = k_i\exp\frac{-E_a}{k_i}\left(\frac{1}{T} - \frac{1}{T_{ref}}\right)$	$i \in \{p, s\}$	(A.26)

Declaration of competing interest

The authors declare that they have no known competing financial interests or personal relationships that could have appeared to influence the work reported in this paper.

Data availability

No data was used for the research described in the article.

Appendix A. P2D model

See Tables A.3–A.5.

Appendix B. Supplementary data

Supplementary material related to this article can be found online at https://doi.org/10.1016/j.jpowsour.2023.233378.

References

[1] A. Somà, F. Bruzzese, F. Mocera, E. Viglietti, Hybridization factor and performance of hybrid electric telehandler vehicle, IEEE Trans. Ind. Appl. 52 (6) (2016) 5130–5138, http://dx.doi.org/10.1109/TIA.2016.2595504.

[2] F. Mocera, E. Vergori, A. Somà, Battery performance analysis for working vehicle applications, IEEE Trans. Ind. Appl. 56 (1) (2019) 644–653.

[3] M. Armand, P. Axmann, D. Bresser, M. Copley, K. Edström, C. Ekberg, D. Guyomard, B. Lestriez, P. Novák, M. Petranikova, et al., Lithium-ion batteries–Current state of the art and anticipated developments, J. Power Sources 479 (2020) 228708.

[4] M. Marinaro, D. Bresser, E. Beyer, P. Faguy, K. Hosoi, H. Li, J. Sakovica, K. Amine, M. Wohlfahrt-Mehrens, S. Passerini, Bringing forward the development of battery cells for automotive applications: Perspective of R&D activities in China, Japan, the EU and the USA, J. Power Sources 459 (2020) 228073.

[5] M. Kabir, D.E. Demirocak, Degradation mechanisms in Li-ion batteries: a state-of-the-art review, Int. J. Energy Res. 41 (14) (2017) 1963–1986.

[6] M. Woody, M. Arbabzadeh, G.M. Lewis, G.A. Keoleian, A. Stefanopoulou, Strategies to limit degradation and maximize Li-ion battery service lifetime-critical review and guidance for stakeholders, J. Energy Storage 28 (2020) 101231.

[7] F. Mocera, A. Somà, D. Clerici, Study of aging mechanisms in lithium-ion batteries for working vehicle applications, in: 2020 Fifteenth International Conference on Ecological Vehicles and Renewable Energies, EVER, IEEE, 2020, pp. 1–8.

[8] R. Deshpande, Y.-T. Cheng, M.W. Verbrugge, Modeling diffusion-induced stress in nanowire electrode structures, J. Power Sources 195 (15) (2010) 5081–5088.

[9] Y. Zhao, P. Stein, Y. Bai, M. Al-Siraj, Y. Yang, B.-X. Xu, A review on modeling of electro-chemo-mechanics in lithium-ion batteries, J. Power Sources 413 (2019) 259–283.

[10] D. Clerici, F. Mocera, A. Somà, Analytical solution for coupled diffusion induced stress model for lithium-ion battery, Energies 13 (7) (2020) http://dx.doi.org/10.3390/en13071717.

[11] D. Clerici, F. Mocera, A. Somà, Shape influence of active material micro-structure on diffusion and contact stress in lithium-ion batteries, Energies 14 (1) (2021).

[12] D. Clerici, F. Mocera, Micro-scale modeling of lithium-ion battery, IOP Conf. Ser. Mater. Sci. Eng. 1038 (1) (2021) 012007.

[13] D. Clerici, F. Mocera, A. Somà, Experimental characterization of lithium-ion cell strain using laser sensors, Energies 14 (19) (2021).

[14] C.R. Birkl, M.R. Roberts, E. McTurk, P.G. Bruce, D.A. Howey, Degradation diagnostics for lithium ion cells, J. Power Sources 341 (2017) 373–386.

[15] D. Lyu, B. Ren, S. Li, Failure modes and mechanisms for rechargeable lithium-based batteries: a state-of-the-art review, Acta Mech. 230 (2019) 701–727.

[16] J.S. Edge, S. O'Kane, R. Prosser, N.D. Kirkaldy, A.N. Patel, A. Hales, A. Ghosh, W. Ai, J. Chen, J. Yang, et al., Lithium ion battery degradation: what you need to know, Phys. Chem. Chem. Phys. 23 (14) (2021) 8200–8221.

[17] J. Christensen, Modeling diffusion-induced stress in Li-ion cells with porous electrodes, J. Electrochem. Soc. 157 (3) (2010) A366.

[18] Y.-T. Cheng, M.W. Verbrugge, Evolution of stress within a spherical insertion electrode particle under potentiostatic and galvanostatic operation, J. Power Sources 190 (2) (2009) 453–460.

[19] X. Zhang, W. Shyy, A.M. Sastry, Numerical simulation of intercalation-induced stress in Li-ion battery electrode particles, J. Electrochem. Soc. 154 (10) (2007) A910.

[20] R. Grantab, V.B. Shenoy, Pressure-gradient dependent diffusion and crack propagation in lithiated silicon nanowires, J. Electrochem. Soc. 159 (5) (2012) A584–A591.

[21] M. Klinsmann, D. Rosato, M. Kamlah, R.M. Mcmeeking, Modeling crack growth during Li insertion in storage particles using a fracture phase field approach, J. Mech. Phys. Solids 92 (2016) 313–344.

[22] A. Mesgarnejad, A. Karma, Phase field modeling of chemomechanical fracture of intercalation electrodes: Role of charging rate and dimensionality, J. Mech. Phys. Solids 132 (2019) 1–20.

[23] R. Xu, K. Zhao, Corrosive fracture of electrodes in Li-ion batteries, J. Mech. Phys. Solids 121 (2018) 258–280.

[24] L. Yang, H.-S. Chen, H. Jiang, W.-L. Song, D. Fang, Lithium redistribution around the crack tip of lithium-ion battery electrodes, Scr. Mater. 167 (2019) 11–15.

[25] P. Li, Y. Zhao, Y. Shen, S.H. Bo, Fracture behavior in battery materials, J. Phys. Energy 2 (2) (2020).

[26] F. Pistorio, D. Clerici, F. Mocera, A. Somà, Review on the experimental characterization of fracture in active material for lithium-ion batteries, Energies 15 (23) (2022) 9168.

[27] N. Lin, Z. Jia, Z. Wang, H. Zhao, G. Ai, X. Song, Y. Bai, V. Battaglia, C. Sun, J. Qiao, et al., Understanding the crack formation of graphite particles in cycled commercial lithium-ion batteries by focused ion beam-scanning electron microscopy, J. Power Sources 365 (2017) 235–239.

[28] K.-J. Park, J.-Y. Hwang, H.-H. Ryu, F. Maglia, S.-J. Kim, P. Lamp, C.S. Yoon, Y.-K. Sun, Degradation mechanism of Ni-enriched NCA cathode for lithium batteries: are microcracks really critical? ACS Energy Lett. 4 (6) (2019) 1394–1400.

[29] S.W. Lee, M.T. McDowell, L.A. Berla, W.D. Nix, Y. Cui, Fracture of crystalline silicon nanopillars during electrochemical lithium insertion, Proc. Natl. Acad. Sci. 109 (11) (2012) 4080–4085.

[30] F. Pistorio, D. Clerici, F. Mocera, A. Somà, Review on the numerical modeling of fracture in active materials for lithium ion batteries, J. Power Sources 566 (2023) 232875.

[31] W.H. Woodford, Y.-M. Chiang, W.C. Carter, Electrochemical shock" of intercalation electrodes: a fracture mechanics analysis, J. Electrochem. Soc. 157 (10) (2010) A1052.

[32] R.S. Raghavan, A.M. Kumar, R. Narayanrao, Intercalation induced surface cracking in electrode particles, ZAMM Z. Angew. Math. Mech. 95 (8) (2015) 845–858.

[33] B. Chen, J. Zhou, R. Cai, Analytical model for crack propagation in spherical nano electrodes of lithium-ion batteries, Electrochim. Acta 210 (2016) 7–14.

[34] A. Sarkar, P. Shrotriya, A. Chandra, Fracture modeling of lithium-silicon battery based on variable elastic moduli, J. Electrochem. Soc. 164 (11) (2017) E3606.

[35] D. Clerici, F. Mocera, F. Pistorio, Analysis of fracture behaviour in active materials for lithium ion batteries, IOP Conf. Ser. Mater. Sci. Eng. 1214 (1) (2022) 012018.

[36] Y.F. Gao, M. Zhou, Coupled mechano-diffusional driving forces for fracture in electrode materials, J. Power Sources 230 (2013) 176–193.

[37] H. Haftbaradaran, J. Qu, A path-independent integral for fracture of solids under combined electrochemical and mechanical loadings, J. Mech. Phys. Solids 71 (1) (2014) 1–14.

[38] M. Zhang, J. Qu, J.R. Rice, Path independent integrals in equilibrium electro-chemo-elasticity, J. Mech. Phys. Solids 107 (2017) 525–541.

[39] I. Ryu, J.W. Choi, Y. Cui, W.D. Nix, Size-dependent fracture of Si nanowire battery anodes, J. Mech. Phys. Solids 59 (9) (2011) 1717–1730, http://dx.doi.org/10.1016/j.jmps.2011.06.003.

[40] R. Grantab, V.B. Shenoy, Location-and orientation-dependent progressive crack propagation in cylindrical graphite electrode particles, J. Electrochem. Soc. 158 (8) (2011) A948.

[41] G. Sun, T. Sui, B. Song, H. Zheng, L. Lu, A.M. Korsunsky, On the fragmentation of active material secondary particles in lithium ion battery cathodes induced by charge cycling, Extreme Mech. Lett. 9 (2016) 449–458.

[42] Y. Zhang, Z. Guo, Numerical computation of central crack growth in an active particle of electrodes influenced by multiple factors, Acta Mech. Sinica 34 (2018) 706–715.

[43] Y. Zhang, C. Zhao, Z. Guo, Simulation of crack behavior of secondary particles in Li-ion battery electrodes during lithiation/de-lithiation cycles, Int. J. Mech. Sci. 155 (2019) 178–186.

[44] A. Singh, S. Pal, Coupled chemo-mechanical modeling of fracture in polycrystalline cathode for lithium-ion battery, Int. J. Plast. 127 (2020) 102636.

[45] Y. Bai, K. Zhao, Y. Liu, P. Stein, B.-X. Xu, A chemo-mechanical grain boundary model and its application to understand the damage of Li-ion battery materials, Scr. Mater. 183 (2020) 45–49.

[46] H. Tian, L. Gao, P. Huang, Y. Li, Z.-S. Guo, Simulation of intergranular fracture behavior inside randomly aggregated LiNixCoyMn1-x-yO2 polycrystalline particle, Eng. Fract. Mech. 266 (2022) 108381.

[47] C. Miehe, H. Dal, L.-M. Schänzel, A. Raina, A phase-field model for chemo-mechanical induced fracture in lithium-ion battery electrode particles, Internat. J. Numer. Methods Engrg. 106 (9) (2016) 683–711.

[48] M. Ahmadi, A hybrid phase field model for fracture induced by lithium diffusion in electrode particles of Li-ion batteries, Comput. Mater. Sci. 184 (2020) 109879.

[49] A. Singh, S. Pal, Chemo-mechanical modeling of inter-and intra-granular fracture in heterogeneous cathode with polycrystalline particles for lithium-ion battery, J. Mech. Phys. Solids 163 (2022) 104839.

[50] R. Xue, X. Li, H. Zhao, Z. Chen, Phase field model coupling with strain gradient plasticity for fracture in lithium-ion battery electrodes, Eng. Fract. Mech. 269 (2022) 108518.

[51] W. Ai, B. Wu, E. Martínez-Pañeda, A coupled phase field formulation for modelling fatigue cracking in lithium-ion battery electrode particles, J. Power Sources 544 (2022) 231805.

[52] M. Klinsmann, D. Rosato, M. Kamlah, R.M. McMeeking, Modeling crack growth during Li insertion in storage particles using a fracture phase field approach, J. Mech. Phys. Solids 92 (2016) 313–344.

[53] A. Mesgarnejad, A. Karma, Phase field modeling of chemomechanical fracture of intercalation electrodes: Role of charging rate and dimensionality, J. Mech. Phys. Solids 132 (2019) 103696.

[54] A.M. Boyce, E. Martínez-Pañeda, A. Wade, Y.S. Zhang, J.J. Bailey, T.M. Heenan, D.J. Brett, P.R. Shearing, Cracking predictions of lithium-ion battery electrodes by X-ray computed tomography and modelling, J. Power Sources 526 (2022) 231119.

[55] D. T O'Connor, M.J. Welland, W.K. Liu, P.W. Voorhees, Phase transformation and fracture in single LixFePO4 cathode particles: a phase-field approach to Li–ion intercalation and fracture, Modelling Simul. Mater. Sci. Eng. 24 (3) (2016) 035020.

[56] B. Liu, J. Xu, Cracks of silicon nanoparticles in anodes: Mechanics–electrochemical-coupled modeling framework based on the phase-field method, ACS Appl. Energy Mater. 3 (11) (2020) 10931–10939.

[57] B.-X. Xu, Y. Zhao, P. Stein, Phase field modeling of electrochemically induced fracture in Li-ion battery with large deformation and phase segregation, GAMM-Mitt. 39 (1) (2016) 92–109.

[58] T.F. Fuller, M. Doyle, J. Newman, Simulation and optimization of the dual lithium ion insertion cell, J. Electrochem. Soc. 141 (1) (1994) 1.

[59] D. Clerici, F. Mocera, A. Somà, Analytical solution for coupled diffusion induced stress model for lithium-ion battery, Energies 13 (7) (2020) 1717.

[60] J.R. Rice, A path independent integral and the approximate analysis of strain concentration by notches and cracks, J. Appl. Mech. 35 (2) (1968) 379–386.

[61] S. Aoki, K. Kishimoto, M. Sakata, Elastic-plastic analysis of crack in thermally-loaded structures, Eng. Fract. Mech. 16 (3) (1982) 405–413.

[62] K. Kishimoto, S. Aoki, M. Sakata, On the path independent integral- j, Eng. Fract. Mech. 13 (4) (1980) 841–850.

[63] M. Torchio, L. Magni, R.B. Gopaluni, R.D. Braatz, D.M. Raimondo, LIONSIMBA: A matlab framework based on a finite volume model suitable for Li-ion battery design, simulation, and control, J. Electrochem. Soc. 163 (7) (2016) A1192–A1205.

[64] C.F. Shih, B. Moran, T. Nakamura, Energy release rate along a three-dimensional crack front in a thermally stressed body, Int. J. Fract. 30 (2) (1986) 79–102.

[65] E.J. Cheng, N.J. Taylor, J. Wolfenstine, J. Sakamoto, Elastic properties of lithium cobalt oxide (LiCoO2), J. Asian Ceram. Soc. 5 (2) (2017) 113–117.

[66] F. Jiang, P. Peng, Elucidating the performance limitations of lithium-ion batteries due to species and charge transport through five characteristic parameters, Sci. Rep. 6 (1) (2016) 32639.

[67] S. Tang, Z. Wang, H. Guo, J. Wang, X. Li, G. Yan, Systematic parameter acquisition method for electrochemical model of 4.35 V LiCoO2 batteries, Solid State Ion. 343 (2019) 115083.

[68] J. Christensen, J. Newman, Stress generation and fracture in lithium insertion materials, J. Solid State Electrochem. 10 (5) (2006) 293–319.

[69] Y. Song, X. Shao, Z. Guo, J. Zhang, Role of material properties and mechanical constraint on stress-assisted diffusion in plate electrodes of lithium ion batteries, J. Phys. D: Appl. Phys. 46 (10) (2013) 105307.

[70] B. Rieger, S.V. Erhard, K. Rumpf, A. Jossen, A new method to model the thickness change of a commercial pouch cell during discharge, J. Electrochem. Soc. 163 (8) (2016) A1566.

[71] A.H. Wiedemann, G.M. Goldin, S.A. Barnett, H. Zhu, R.J. Kee, Effects of three-dimensional cathode microstructure on the performance of lithium-ion battery cathodes, Electrochim. Acta 88 (2013) 580–588.

[72] P.W. Northrop, V. Ramadesigan, S. De, V.R. Subramanian, Coordinate transformation, orthogonal collocation, model reformulation and simulation of electrochemical-thermal behavior of lithium-ion battery stacks, J. Electrochem. Soc. 158 (12) (2011) A1461.

[73] W. Fang, P. Ramadass, Z.J. Zhang, Study of internal short in a Li-ion cell-II. Numerical investigation using a 3D electrochemical-thermal model, J. Power Sources 248 (2014) 1090–1098.

[74] M. Doyle, Y. Fuentes, Computer simulations of a lithium-ion polymer battery and implications for higher capacity next-generation battery designs, J. Electrochem. Soc. 150 (6) (2003) A706.

[75] K. Takahashi, V. Srinivasan, Examination of graphite particle cracking as a failure mode in lithium-ion batteries: a model-experimental study, J. Electrochem. Soc. 162 (4) (2015) A635.

[76] W. Ai, L. Kraft, J. Sturm, A. Jossen, B. Wu, Electrochemical thermal-mechanical modelling of stress inhomogeneity in lithium-ion pouch cells, J. Electrochem. Soc. 167 (1) (2020) 013512.

[77] R. Ruess, S. Schweidler, H. Hemmelmann, G. Conforto, A. Bielefeld, D.A. Weber, J. Sann, M.T. Elm, J. Janek, Influence of NCM particle cracking on kinetics of lithium-ion batteries with liquid or solid electrolyte, J. Electrochem. Soc. 167 (10) (2020) 100532.
[78] S. Xia, L. Mu, Z. Xu, J. Wang, C. Wei, L. Liu, P. Pianetta, K. Zhao, X. Yu, F. Lin, et al., Chemomechanical interplay of layered cathode materials undergoing fast charging in lithium batteries, Nano Energy 53 (2018) 753–762.
[79] D. Clerici, F. Mocera, A. Somà, Electrochemical–mechanical multi-scale model and validation with thickness change measurements in prismatic lithium-ion batteries, J. Power Sources 542 (2022) 231735.
[80] T.L. Anderson, Fracture Mechanics: Fumdamental and Applications, 2017, p. 668.
[81] G. Sun, S. Bhattacharya, A. Alpas, Cyclic strain-induced crack growth in graphite during electrochemical testing in propylene carbonate-based Li-ion battery electrolytes, J. Mater. Sci. 53 (2) (2018) 1297–1309.
[82] J.G. Swallow, W.H. Woodford, F.P. McGrogan, N. Ferralis, Y.-M. Chiang, K.J. Van Vliet, Effect of electrochemical charging on elastoplastic properties and fracture toughness of LiXCoO2, J. Electrochem. Soc. 161 (11) (2014) F3084.
[83] D. Chen, D. Kramer, R. Mönig, Chemomechanical fatigue of LiMn1. 95Al0. 05O4 electrodes for lithium-ion batteries, Electrochim. Acta 259 (2018) 939–948.
[84] G. Li, Z. Zhang, Z. Huang, C. Yang, Z. Zuo, H. Zhou, Understanding the accumulated cycle capacity fade caused by the secondary particle fracture of LiNi 1-xy Co x Mn y O 2 cathode for lithium ion batteries, J. Solid State Electrochem. 21 (2017) 673–682.
[85] K. Zhao, M. Pharr, J.J. Vlassak, Z. Suo, Fracture of electrodes in lithium-ion batteries caused by fast charging, J. Appl. Phys. 108 (7) (2010) 073517.
[86] A. Hitt, F. Wang, Z. Li, M. Ge, Y. Zhang, Y. Savsatli, X. Xiao, W.-K. Lee, R. Stephens, M. Tang, Nanotomographic observation and statistical analysis of overcharging induced cracks in LiCoO2 single crystalline particles, Energy Storage Mater. 52 (2022) 320–328.
[87] J. Zhang, J. Qiao, K. Sun, Z. Wang, Balancing particle properties for practical lithium-ion batteries, Particuology 61 (2022) 18–29.
[88] J. Zheng, X. Wu, Y. Yang, A comparison of preparation method on the electrochemical performance of cathode material Li [Li0. 2Mn0. 54Ni0. 13Co0. 13] O2 for lithium ion battery, Electrochim. Acta 56 (8) (2011) 3071–3078.